UCRL-50007-75-1

HAZARDS CONTROL PROGRESS REPORT NO. 50

January through June 1975

August 15, 1975

Prepared for U.S. Energy Research & Development Administration under contract No. W-7405-Eng-48

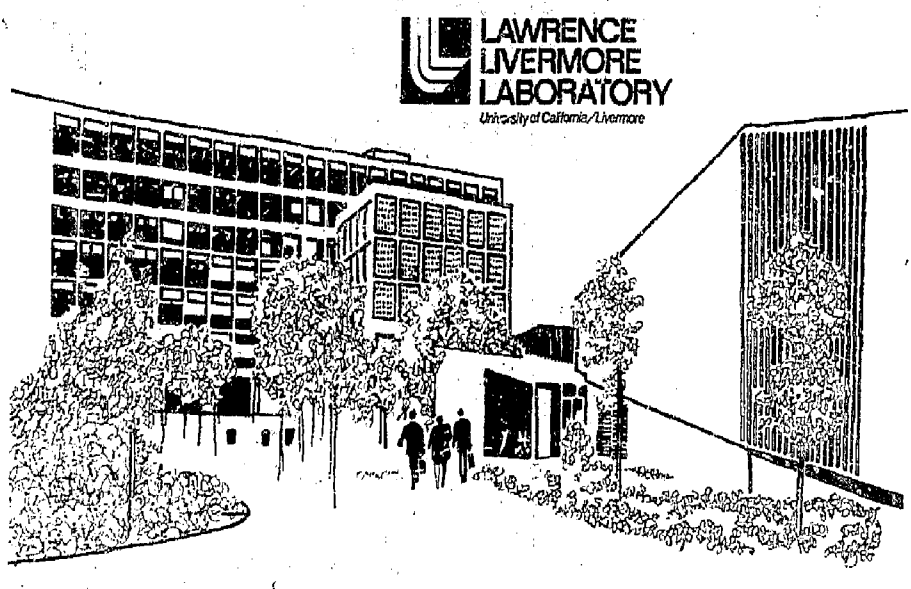

Printed in the United States of America
Available from
National Technical Information Service
U. S. Department of Commerce
5285 Port Royal Road
Springfield, Virginia 22151
Price: Printed Copy $___*; Microfiche $2.25

*Pages	NTIS Selling Price
1-50	$4.00
51-150	$5.45
151-325	$7.60
326-500	$10.60
501-1000	$13.60

Distribution Category
UC-41

LAWRENCE LIVERMORE LABORATORY
University of California Livermore, California 94550

UCRL-50007-75-1

HAZARDS CONTROL PROGRESS REPORT NO. 50

January through June 1975

MS. date: August 15, 1975

Contents

PROGRESS REPORTS

TECHNICAL NOTES

Edited by V. R. Mendenhall

Progress Reports

RADIATION PROTECTION

Theoretical Studies of X-ray Attenuation in a Simulated Chest Wall

Introduction. LLL is committed to a continuing program to improve the sensitivity and precision of the whole-body counter to detect and quantify plutonium in the lungs. Measurements are now made using two 12.7-cm-diam NaI(Tl) detectors which count plutonium L x rays passing through the chest wall. Since these x rays occur at low energy (three principal groups at 13.6, 17, and 20.2 keV) the measurements are severely constrained by attenuation in the chest wall.

The chest wall surrounding the lungs may be up to 4.5 cm thick which amounts to three to seven mean free path lengths at 13.0 keV. The quality of present plutonium lung burden measurements is limited by three primary considerations:

- Uncertainty in the spatial distribution of plutonium in the lungs.
- Effects of the counting geometry on detection efficiency.
- Attenuation in the chest wall.

A theoretical study is now underway to obtain some degree of understanding of the role played by each of these effects. As yet, only chest wall attentuation has been looked at in detail, and that work is not complete. However, some very preliminary data will be reported here.

Experiments. Estimates of chest wall attenuation are made in the following way: A lung is simulated by a phantom of Remab material molded in the shape of a lung (see Fig. 1). The material is doped uniformly with plutonium or ^{103}Pd which decays to produce two Rh x-ray groups at 20 and 23 keV. A chest wall is simulated by placing various thicknesses of beefsteak over the lung. The detector is then positioned to measure the count rate due to photons in the energy range 13-30 keV which reach the detector.

Theoretical Studies. There are a number of ways to calculate chest wall attenuation, incorporating various degrees of sophistication. The simplest calculation would be one which assumes a transmission varying exponentially with thickness. Such a calculation would be valid only so long as the following requirements were satisfied, at least approximately: (1) Monoenergetic photons, (2) non-scattering materials, (3) all photons incident at the same angle.

None of the above conditions are satisfied, even approximately, in the problem being considered. However, condition (1) above may be relaxed easily by taking a linear superposition of transmitted intensities due to each individual photon energy group incident on the chest wall. In the case where there are basically three groups of x rays, the intensity transmitted through the chest wall is given by

$$\frac{I(x)}{I_0} = \frac{I_1 e^{-\mu_1 x} + I_2 e^{-\mu_2 x} + I_3 e^{-\mu_3 x}}{I_1 + I_2 + I_3}$$

where I_i are the intensities of each group incident on the chest wall and μ_i the respective attenuation coefficients. I_0 is the total incident intensity, $I_0 = I_1 + I_2 + I_3$.

Similarly, condition (2) above may be relaxed by defining an appropriate "buildup factor" for the problem being considered, i.e.,

$$B(x) = \frac{\phi(x)_{\text{total}}}{\phi(x)_{\text{unscat}}}$$

where $\phi(x)_{\text{unscat}}$ is the photon intensity at position x in the attenuator due to

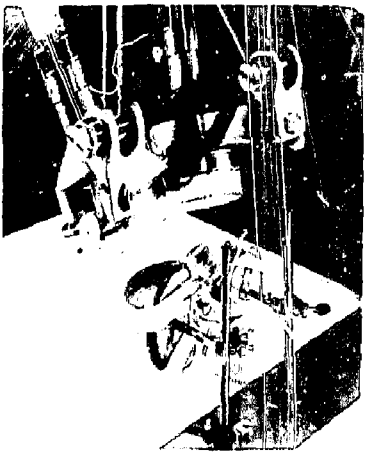

Fig. 1. Simulated lung.

photons which have not yet undergone any interactions, and

$\phi(x)_{total}$ is the total intensity at position x of photons with energies within the detector acceptance window, including those which have scatte.ed.

Clearly, B(x) will depend upon the incident photon energy, thickness of material, detector energy window, and it will be shown that it depends somewhat on geometrical considerations other than thickness of material. A crude calculation with restraints (1) and (2) relaxed would be of the form:

$$\frac{I}{I_0} = \frac{I_1 B_1(x) e^{-\mu_1 x} + I_2 B_2(x) e^{-\mu_2 x} + I_3 B_3(x) e^{-\mu_3 x}}{I_1 + I_2 + I_3}$$

where $B_i(x)$ are the buildup factors for the respective source energy groups. One still has the problem of calculating $B_i(x)$ for each photon group. However, B(x) varies much less rapidly in tissue than does the exponential $e^{-\mu x}$ and so it may be represented in good approximation by a simple polynomial. Part of the present work involves modelling the variation of buildup as a function of source energy and tissue thickness. That effort is not yet complete.

A more sophisticated calculation must deal with the angular distribution of incident photons and the dimensions other than chest wall thickness which affect the probability that a photon will scatter into the detector. Figure 2 shows graphically that the path length of a photon through the chest wall varies widely. The mean path length over this distribution depends significantly on the size and separation of the lung and detector. Thus the chest wall attenuation is

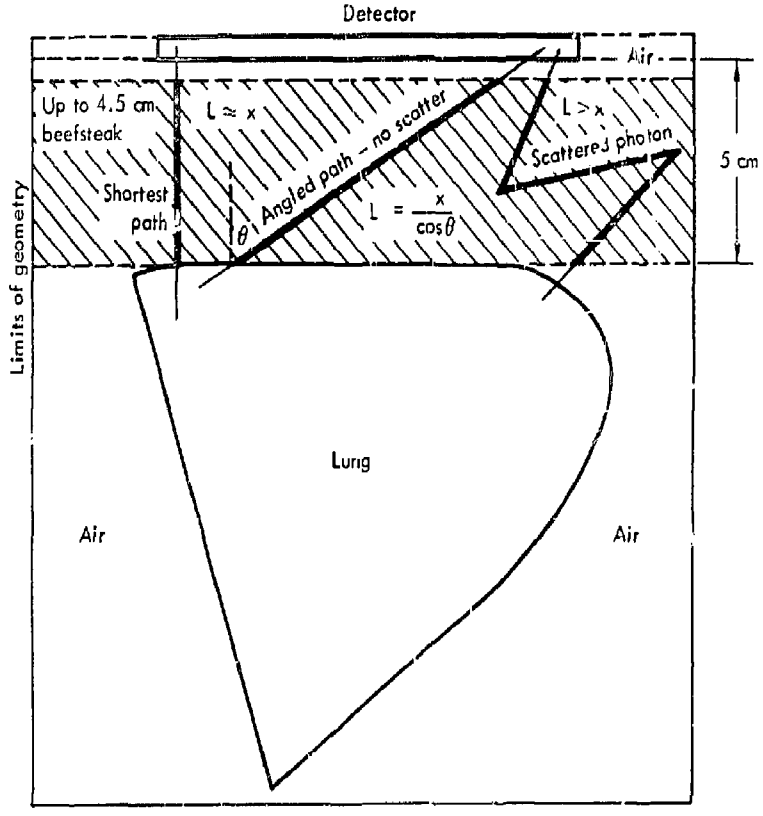

Fig. 2. Path length and thus attenuation is very much geometry-dependent. Variation of path length of photons through chest wall.

dependent upon all of the dimensions in the chest wall – detector geometry.

Monte Carlo Calculations. The Monte Carlo code MORSE has been used to calculate the photon detection rate in the detector, above 13 keV, for various thicknesses of simulated chest wall and for several counting geometries.

A single detector was assumed to be 5 cm above a single lung. The detector count rate was calculated for simulated chest wall thicknesses of 0, 1, 2, 3, 4, 4.5 cm and the results normalized to those for zero thickness. Calculations were carried out for a plutonium source distributed uniformly over the lung and assumed branching intensities of 0.363, 0.517 and 0.12 for the 13.6-, 17-, and 20.2-keV x-ray groups. Similar calculations were done for a ^{103}Pd source where the branching intensities were assumed 0.830, 0.147 and 0.022 for the 20.2-, 22.7-, and 23.1-keV groups.

Results. Figure 3 shows the results as a function of beefsteak (simulated chest wall) thickness. The solid curves give the total number of photons detected with energies above the detector threshold. Dashed curves correspond to the number of detected photons which underwent no interactions in either the lung or simulated chest wall. The difference between corresponding solid and dashed curves indicates the contribution to the detection rate arising from photons which scattered at least once in the lung or chest wall, but reached the detector at any energy above its threshold.

Figure 4 shows the effective buildup factor as a function of chest wall thickness for the incident energy spectrum assumed. The figure shows that scattered photons may enhance the detection rate up to 50% for the geometry considered. It is also interesting to note that the scattering contributes to a small intensity buildup within the lung itself.

Conclusions. These preliminary results show the importance of including buildup due to scattering in calculating the attenuation of chest wall material. Initial investigations indicate that source detector geometry and spatial distribution of the source are also important. Calculations are continuing to study these effects with a view to modelling the system response to changes in geometry or spatial distribution as well as changes in the detector energy acceptance window.

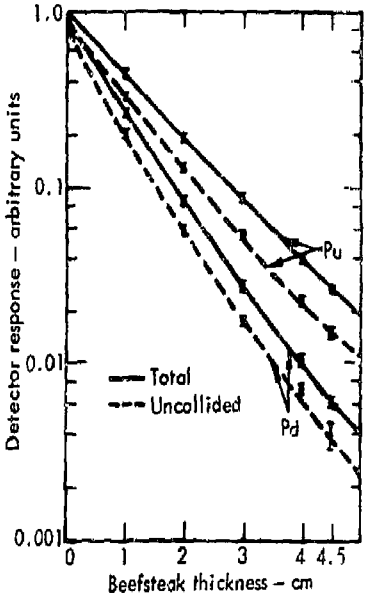

Fig. 3. Detector response versus simulated chest wall thickness.

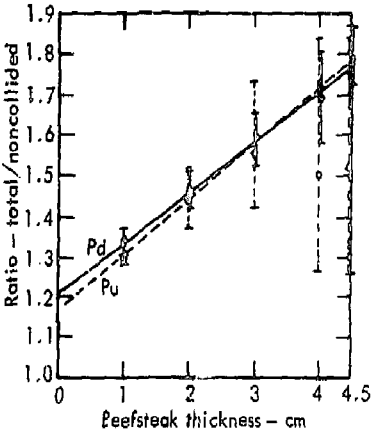

Fig. 4. Effective buildup factor versus simulated chest wall thickness.

Response of the LLL Personnel TLD Badge to Penetrating and Nonpenetrating Radiation

Introduction. The allowable exposure limits for nonpenetrating radiation are several times higher than the limits for penetrating radiations. Most personnel dosimeters are designed to measure the penetrating and nonpenetrating doses separately. Unfortunately until now, no definition of penetrating and nonpenetrating has been given, and existing personnel dosimeters very greatly. Some dosimeters are designed to measure the

penetrating component of the dose at tissue depths equivalent to the bone (5 cm) while others measure the dose at tissue depths of 1-, 2-, 2.5- or 3-cm depth.

A joint ICRP-ICRU committee exists which is in the process of producing a document, "Conceptual Basis for Radiation Protection" which will be submitted for review shortly. Their recommendation will be based on the "restricted dose-equivalent indices." This consists of a sphere 30 cm in diameter of tissue-equivalent material. An outer shell 7 mg/cm^2 thick would correspond to the dead layer of skin, followed by a shell approximately 1 cm thick for specifying skin dose equivalent, and finally the main body of the sphere about 28 cm in diameter in which the dose to the gonads and blood-forming organs will be specified. The MADE (Maximum Absorbed Dose Equivalent) index restricted to the 28-cm-diam inner sphere will be set at 5 rem/y, that for the 1-cm shell at 30 rem/y. The value for the eye will be left at 15 rem/y as the ICRP has it now. (Chapter 0524 limits are 5 rem/y for the whole body and lens of the eye and 15 rem/y for skin exposures.)

If the above document is accepted, penetrating and nonpenetrating doses will be defined. For nonpenetrating exposures a dosimeter should measure the dose in the first cm of tissue, and for penetrating exposures the dose at depths of greater than 1 cm. Both the nonpenetrating and penetrating doses will vary at increasing depths, being higher near the surface and at 1 cm and decreasing as the depth approaches 1 cm or the center of the sphere (assuming isotropic exposure). A dosimeter probably should be designed to measure the highest dose (which would be near the surface for nonpenetrating and at the 1 cm interface for penetrating radiation). This would provide a dose measurement which would always be conservative.

A study was made of the LLL personnel TLD dosimeter system to determine how well it would meet the above criteria. It was felt that the dosimeter presently used to measure the "penetrating" dose was probably undershielded and was measuring at an equivalent tissue depth of less than 1 cm.

Procedure. Exposures of the LLL personnel TLD badges were made to fluorescent x-ray energies of 11, 23 and 32 keV, ^{137}Cs gamma rays, and to beta particles from a ^{90}Sr source. All exposures were made with the badge placed on a 4-in.-thick Lucite phantom used to provide the backscatter of low-energy x rays. This backscatter is very large at some of the lower x-ray energies (see Ref. 1). The exposures for each x-ray energy were made under the same conditions and to the same dose.

The personnel TLD badges are worn under a security badge made of polypropylene. In this study, the following exposures were made: (1) without the security badge (to simulate the open window nonpenetrating reading of the badge); (2) with the security badge over the TLD's (to simulate the present penetrating readings); (3) with aluminum 16, 20, 25, 31, 55 and 62.5 mils thick placed between the security badge and the TLD's; and (4) with Lucite 1/16, 1/8 and 3/16 in. thick placed on top of the security badge.

To determine the dose at a depth of 1 cm in tissue, TLD's were placed in glassine envelopes and taped to the phantom. Tissue-equivalent plastic (Rando) sheets 0.5, 1, 2 and 3 cm thick were placed between the TLD's and the sources to obtain a relative depth dose measurement. The results obtained are given in Table 1. In Table 2, the results are normalized to the unshielded TLD readings.

Figure 5 shows the results in Table 2 plotted as a function of thickness of Al and Lucite. The zero intercept of the curves is not at 1 because the security badge provides significant shielding compared to the unshielded badge reading (open window). The Lucite provides little shielding for the 23- and 32-keV x rays, but is significant for the 11-keV x rays and the ^{90}Sr beta. The aluminum provides significant shielding for all x-ray energies and for the beta particles.

Figure 6 shows the depth dose curves that one obtains with the Rando tissue-equivalent plastic. The ^{137}Cs curve lies above "1" because the TLD readings with no absorber (open window) gave a lower reading than the TLD readings behind the plastic (probably because electron equilibrium had not been established in the air).

Discussion. The desired response of the personnel badge to x rays is to measure the dose at an equivalent depth of 1 cm in tissue. Figure 6 indicates that at 1-cm depth, attenuation values of 0.070, 0.67, and 0.78 are obtained for the 11-, 23- and 32-keV x rays respectively. These values are greater than the values of 0.047, 0.58 and 0.71 which we observed for the TLD's shielded by the security badge alone. The present TLD badge attenuation corresponds to about a depth of 1.4 cm in tissue (see Fig. 6). Therefore, since we are already measuring at an equivalent depth dose of 1.4 cm, it is not necessary to add additional shielding to our badge to discriminate between penetrating and nonpenetrating x rays.

The results for the ^{90}Sr source (Table 2 and Figure 6) indicate that none of the ^{90}Sr is detected at the 1-cm tissue depth, but with the present badge approximately 49% of the beta dose from ^{90}Sr is being measured as a penetrating dose by the shielded TLD. A filter of Lucite or similar material should be used to reduce the beta sensitivity of the dosimeter. The thickness of the filter is limited by what would be practical. Table 2 indicates that the beta being detected by the TLD's for Lucite thicknesses of 3/16,

1/8, and 1/16 in. are 0.5, 5.0 and 15% respectively. The desired beta response is zero, but since it is impractical to use a filter of 3/16 in. or greater thickness, we will have to accept a badge with some overresponse to beta. The extent of this overresponse will depend on the material and the thickness of the filter that is used. Lucite may be too brittle for extended use, and other plastics are being considered.

Fabrication of a Realistic Torso Phantom for Calibration of Heavy-Element Lung Counters

The problem of accurate external measurement of heavy elements, particularly plutonium, in the human lung is made difficult by the unfavorable decay schemes of the isotopes commonly encountered. In the case of plutonium, by far the most abundant photons

Table 1. Readings of TLDs exposed in a Lucite phantom to x rays, gamma rays and beta particles with various shielding placed over the TLDs

	11 keV	23 keV	32 keV	^{137}Cs	^{90}Sr
TLD badge only	6106	20,764	1219	45,486	6127
TLD badge and security badge	286	11,937	861	47,017	2978
TLD badge					
16 mil Al and security badge	66	9566	754	45,446	1415
20 mil Al and security badge	44	8876	728	47,430	1175
31.25 mil Al and security badge	25	7588	711	46,071	964
55 mil Al and security badge	23	5412	585	49,702	252
62.5 mil Al and security badge	22	5044	595	46,001	182
1 16 in. lucite and security badge	79	11,303	910	49,581	940
1 8 in. lucite and security badge	56	10,699	844	49,624	306
3 16 in. lucite and security badge	60	10,127	784	49,274	30
TLDs under Rando plastic					
1 cm	428	13,288	959	52,087	0
2 cm	57	9519	752	49,147	-
3 cm	25	6391	521	45,935	-
0.5 cm	-	-	-		402

Table 2. TLD readings relative to the reading obtained with the TLDs in the badge with no filters (open window)

	11 keV	23 keV	32 keV	^{137}Cs	^{90}Sr
TLD badge only	1.00	1.00	1.00	1.00	1.00
TLD badge and security badge	0.047	0.58	0.71	1.03	0.49
TLD badge.					
16 mil Al and security badge	.011	.46	.62	1.00	.23
20 mil Al and security badge	.0072	.43	.59	1.04	.19
31.25 mil Al and security badge	.0041	.37	.58	1.01	.14
55 mil Al and security badge	.0038	.26	.48	1.09	.041
62.5 mil Al and security badge	.0036	.24	.49	1.01	.030
1/16 in. lucite and security badge	.013	.54	.75	1.00	.15
1/8 in. lucite and security badge	.0092	.52	.69	1.09	.050
3/16 in. lucite and security badge	.0098	.49	.64	1.08	.005
TLDs under Rando plastic					
1 cm	.070	.64	.79	1.15	0
2 cm	.0093	.46	.62	1.08	
3 cm	0.0041	0.31	0.43	1.01	
0.5 cm					0.066

emitted are the L series x rays having an average energy of about 17 keV. The yields are also low – 0.046 x rays per disintegration for ^{239}Pu and 0.115 x rays per disintegration for ^{238}Pu. The plutonium measurement problem is made more difficult by the complex structure of the lungs and overlying ribs and soft tissue. Proper simulation of the human torso for calibration of the large and external counters used for such measurements is extremely difficult.

A recent *in-vivo* lung counter intercomparison effort[2] among a number of laboratories has shown large discrepancies in the activity levels reported. A good part of the problem represented by these discrepancies can be attributed to the lack of an adequate phantom for calibration purposes. For this *reason, the E.R.D.A. has established an intercalibration* Committee for Low-Energy Photon Measurements to develop design criteria for construction of a realistic phantom. The phantom will be built at the Lawrence Livermore Laboratory through a joint effort by the Biomedical Division and the Hazards Control Department.

The Intercalibration Committee has established the following criteria for the phantom:

- It is to be a torso without head, neck or arms, extending to the waist.
- It is to have the stature of an average radiation worker.
- The torso will contain a human male rib cage.
- The organs simulated are to include lungs and

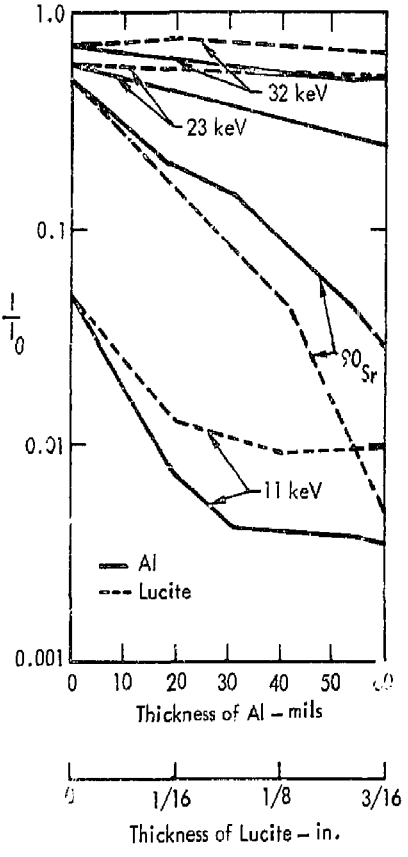

Fig. 5. Relative TLD readings as a function of the thickness of ... and Lucite placed between the badge and th... urce.

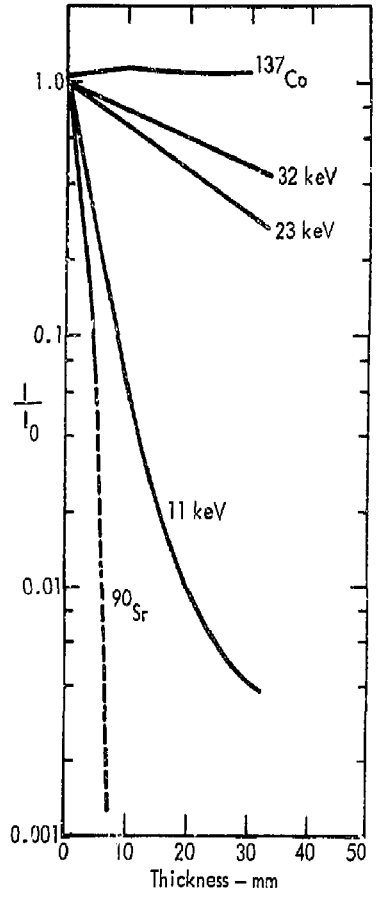

Fig. 6. Relative TLD readings as a function of Kando tissue thickness.

trachea, heart, liver, kidneys and spleen, with provisions for lymph node simulation.

- The materials used for construction will simulate the x ray transmission properties of human tissue with attention given to the differences in x ray transmission between muscle, adipose tissue and cartilage. Material used for the lungs will have a density of about 0,25 g/cm^2.
- The basic phantom is to be constructed with the minimum amount of soft tissue simulant over the lungs necessary for structural strength, but provisions are to be made for simulation of differing amounts of tissue overlying the lung.

Three basic tasks have been involved in the first portion of the phantom construction: (1) Determination of the proper size and shape of the organs as well as the exterior of the torso and the torso cavity without organs; (2) acquisition of the human male rib cage; and (3) investigation of tissue-equivalent materials.

The most available reference with "Standard Man" data[3] reports a weight of 70 kg (155 lb) and a height of 170 cm (5 ft 7 in.), values that were at odds with our experience. An Air Force report[4] contained data for a larger standard man, but one that we suspected as being in better trim than a typical radiation worker. We finally chose to use statistics for employees taken during routine whole-body counts. The result from data for more than 500 LLL and Los Alamos employees was an individual 177 cm (5 ft 10 in.) tall, weighing 76 kg (169 lb) and having a chest circumference of 100 cm (39 in.).

Using that data, we began by enlarging a series of sagittal cross-sectional drawings from an anatomy text[5] to life size. One set of these was pasted to blocks of styrofoam which were cut to the outside contour of the chest. The styrofoam blocks were stacked, aligned with anatomical fiducial points and fastened together (Fig. 7). The assembly was given to a sculptor at the Laboratory who filled out the model with clay and shaped it, based on our dimensions and some photographs taken of one of our employees who has the above dimensions (Fig. 8).

Fig. 7. Styrofoam torso model.

Fig. 8. Clay model (to be used as a guide for shaping the realistic phantom).

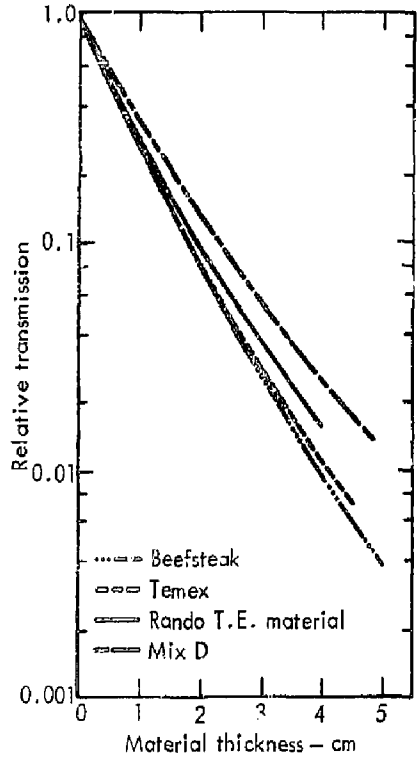

Fig. 9. Transmission of ^{238}Pu L x rays.

We contacted the University of California Medical Center in San Francisco to obtain the rib cage. The office of the Curator of Deceased in the Anatomy Department provided us with the embalmed cadaver of a man 177 cm (5 ft 10 in.) tall, weighing 75 kg (167 lb) and having a chest circumference of 101 cm. After discussions with Dr. Sexton Sutherland, anatomist with the Medical Center, we decided to make a cast of the cadaver, a cast of the torso cavity after removal of the organs, and casts of the major organs themselves. This was done to improve the probability of having the torso and organs in the proper proportion. The chest was cast with conventional surgical plaster tape. The organs were removed and have been retained for future casting. The interior of the torso was cast with an expanding silicon foam which was easily removed after setting. We will make plaster models of the organs, chest and torso void for some final shaping before preparing the phantom casts. The clay model (Fig. 8) will be used as a guide in removing artifacts of the chest resulting from the embalming.

The rib cage has been removed by Dr. Sutherland and cleaned at the Museum of Vertebrate Zoology at the University of California.

Three tissue-equivalent materials have been considered for use in the organs and soft tissue: Temex,[6] Mix-D,[7] and Rando tissue-equivalent material. Transmission measurements with one electroplated source of ^{238}Pu indicate that Temex is closest to the transmission of beefsteak which is used to represent muscle (Fig. 9). This fact plus some structural considerations have led us to prefer the use of Temex for duplication of most of the soft tissue. Since Temex (a depolymerized rubber) is not readily available in the United States, the LLL plastics shop has been assisting us in formulating our own material. The attenuation of plutonium x rays by 4 cm of our current formulation is about a factor of two greater than Temex, so there is more adjustment required in the composition.

With the casts, organs and rib cage necessary for phantom construction, we have come a long way toward fabrication of a realistic phantom. However, a great deal remains to be done including construction of final casts, formulation of the tissue-equivalent material for fat and cartilage as well as muscle, impregnation of the bones with tissue-equivalent material to replace marrow loss, and final phantom construction. The need for the phantom to be used at other laboratories is now such that we are planning to build two more for use in the intercomparison program.

Acknowledgments. We extend our thanks to Dr. Asling, Dr. Sutherland, and Mr. Ritchie of the Anatomy Department, U. C. Medical Center for their assistance in providing us with the anatomical specimens; Mr. Jones, U. C. Museum of Vertebrate Zoology for his help in preparing the rib cage; Dr. Smith, Radiology Department of the U. C. Medical Center for providing samples of Temex; Dr. Rundo, Argonne National Laboratory for providing the Rando T. E. Material; Mr. Boyer and Mr. Striplin of the LLL plastics shop for making the torso casts; Mr. Farsaci of the LLL Technical Information Department for the sculpture; Mr. Fleming of the LLL plastics shop for providing tissue-equivalent material samples for testing; and Mr. Taylor of LLL Hazards Control for preparation of samples of Mix-D as well as general technical support.

Respirator Cartridge Efficiency Studies

Since the last progress report,[8] two additional areas of investigation have been pursued: (1) Additional information has been acquired for cartridge service life as a function of preconditioning and use relative humidity; and (2) the effect of temperature on

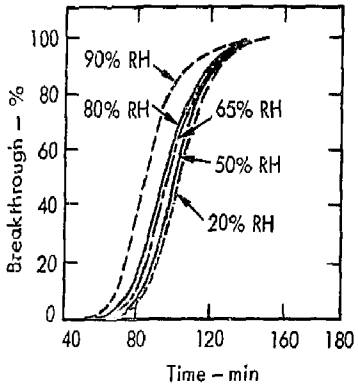

Fig. 10. Breakthrough curves at various use humidities for cartridges preconditioned at 20% R.H.

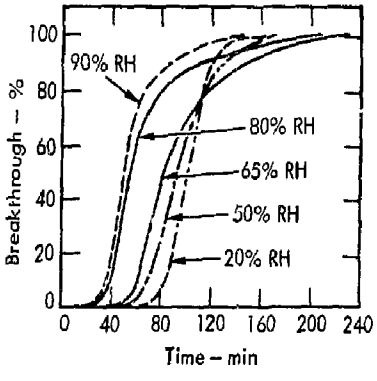

Fig. 11. Breakthrough curves at various use humidities for cartridges preconditioned at 90% R.H.

Table 3. Breakthrough time correction factors at various humidities at 1000 ppm, 53.3 litres/min and 22°C for a pair of cartridges containing coconut or petroleum base carbon. The data have been normalized to the 50% preconditioning and test relative humidity. The letters indicate the test vapor employed and the carbon type. The number in ( ) is the standard deviation

Test relative humidity (%)	Breakthrough time correction factors					
	Preconditioning relative humidity (%)					
	0	20	50	65	80	90
0	0.94 (0.08) FG	0.95 (0.04) BFG	0.99 (0.07) BFG	0.97 (estimated	0.95 (0.07) BFG	0.95 (-) F
20	1.02 (0.06) FG	1.02 (0.03) ACDEFG	1.02 (0.04) ACDEFG	1.04 (0.03) ACDE	1.01 (0.05) ACDEFG	1.00 (0.05) ACDEF
50	0.98 (0.07) BFG	0.99 (0.03) ACDEFG	1.00 (0.05) ABCDEFG	0.99 (0.04) ACDE	0.95 (0.08) ABCDEFG	0.77 (0.20) ABCDEF
65	0.97 (0.04) FG	0.98 (0.04) ACDEFG	0.99 (0.05) ACDEFG	0.94 (0.04) ACDE	0.84 (0.10) ACDEFG	0.66 (0.25) ACDEF
80	0.87 (0.06) BCFG	0.91 (0.05) ACDEFG	0.88 (0.04) ABCDEFG	0.83 (0.09) ACDE	0.72 (0.16) ABCDEFG	0.50 (0.27) ABCDEF
90	0.84 (0.03) CFG	0.85 (0.04) ACDEFG	0.83 (0.06) ACDEFG	0.78 (0.09) ACDE	0.67 (0.13) ACDEFG	0.48 (0.20) ACDEF

A – acetone, petroleum base
B – benzene, petroleum base
C – carbon tetrachloride, coconut base
D – 1-chlorobutane, coconut base
E – ethyl acetate, petroleum base
F – isopropanol, coconut base
G – hexane, coconut base

cartridge efficiency has been calculated from the Mecklenburg Equation.[9]

Effect of Humidity on Cartridge Service Life. Figures 10 and 11 show the breakthrough curves for 1-chlorobutane at various test relative humidities. Some cartridges were preconditioned at 20% RH (Fig. 10) and some were preconditioned at 90% RH (Fig. 11). All cartridges were tested at 1000 ppm, 53.3 litres/min and 22°C. As either the test or storage humidity increases, the service life is diminished.

Table 3 summarizes the data from seven solvents. Using the 50% RH storage and use humidity as a reference point, the service time at other conditions can be approximated using the multipliers provided. It must be remembered, however, that such correction factors vary with activated carbon type and concentration. If the concentration decreases, the water vapor content has a more pronounced effect on the cartridge use time, as shown in the data in Ref. 10.

Effect of Temperature on Cartridge Service Life. At present we do not have the capability to test at various temperatures. Figure 12, however, shows the calculated effect of temperature for seven solvent vapors. These calculations indicate that even over a wide temperature range (0-40°C) the service life is not significantly reduced.

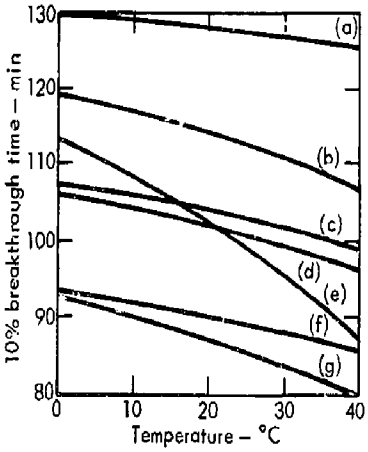

Fig. 12. Calculated effect of temperature on respirator cartridge service life. (a) Perchloroethylene; (b) carbon tetrachloride; (c) ethyl acetate; (d) benzene; (g) pentane.

INSTRUMENT DEVELOPMENT

Improved Electronics Configuration for LLL Neutron Spectrometer System

Development of the LLL Health Physics Neutron Spectrometer System has been described in numerous earlier progress reports[11-15] and some of its details are contained elsewhere in the present report.[16-17] During this development, the electronics configuration has evolved to the point where laboratory neutron energy spectrum measurements are being made routinely with a system whose configuration seems to have stabilized. Results of the measurements appear satisfactory, and so it is likely that this configuration will become permanent.

Our basic spectroscopy system contains two sub-systems, one for scintillation detectors and another for proportional counters. Configuration of the scintillation system used primarily with NE 213 and stilbene detectors is shown in Fig. 13. Pulse shape discrimination is used to suppress analysis of gamma-ray events so that reliable neutron spectrum measurements may be obtained in the energy range 1.0-20 MeV and at count rates up to 3×10^3 sec^{-1}. Less than 1% of the gamma-ray events in the detector leak past the pulse-shape discriminator to contaminate the lowest part of a pulse-height spectrum. Gamma-ray leakage is unimportant at pulse heights greater than that produced by a 1-MeV proton.

The electronics configuration of the proportional counter system is shown in Fig. 14. This system has undergone the greatest evolution since it was last described.

- The best pulse-height analyzer available for some measurements may not have dual parameter capability or even the ability to gate the ADC. A gated linear signal must be available for single parameter analysis.
- Very good risetime resolution is required since the distribution of ^{3}He recoils is narrow in risetime and not well separated from that of the protons produced by ^{3}He(n,p) reactions.
- Gaussian shaping of the linear output with long shaping time constants improves the energy resolution of the system. In addition, good baseline restoration is important in reducing low-frequency noise due to 60-Hz pickup in signal lines and microphonic response of the detectors.

The subsystem shown in Fig. 14 may be used with either a single- or dual-parameter analyzer. Setup for proper pulse-shape discrimination must be determined

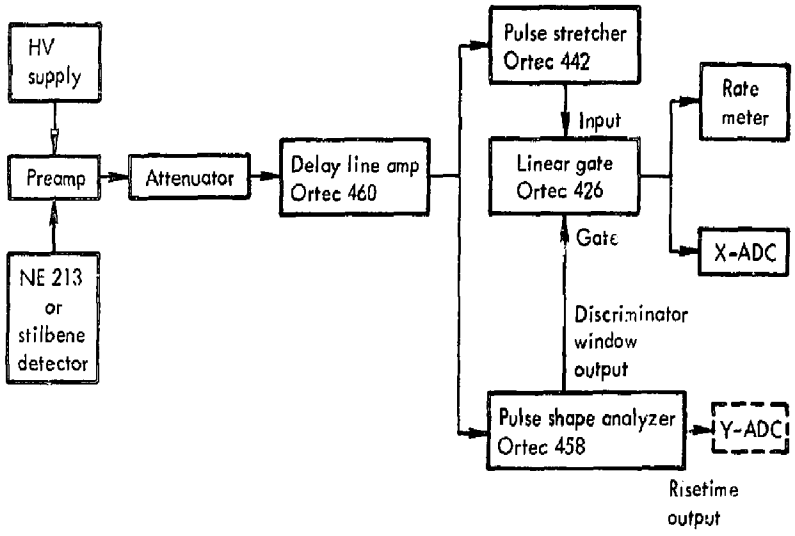

Fig. 13. Electronics configuration for Laboratory Neutron Spectrometer System using scintillation detectors.

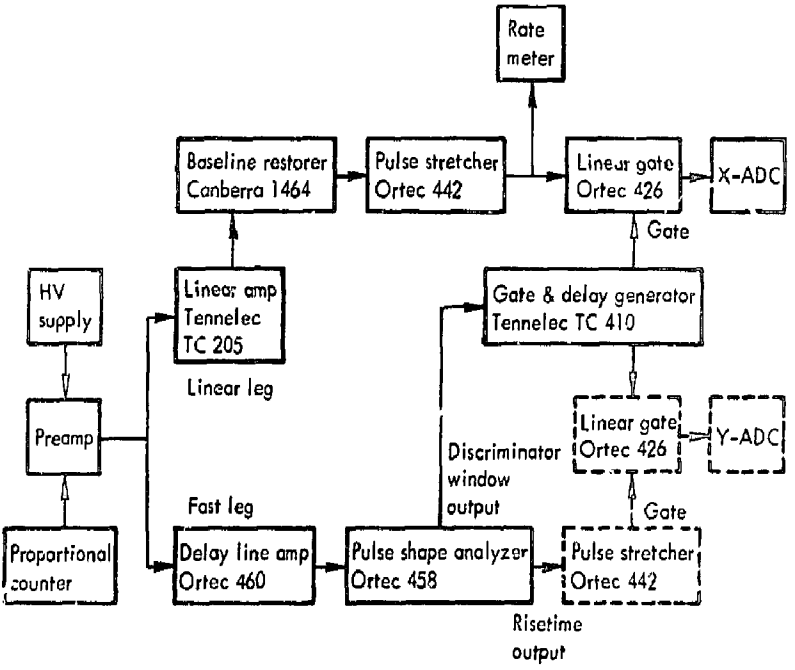

Fig. 14. Electronics configuration for Laboratory Neutron Spectrometer System using proportional counters.

with a dual-parameter analyzer, but once the correct setup is determined a very simple pulse-height analyzer may be used. Analysis of gamma-ray events in hydrogen proportional counters is effectively suppressed so that the pulse-height spectrum is an accurate measure of the proton ionization spectrum in the detector.

Proportional counters containing ^{3}He are more difficult to work with because of the presence of ^{3}He recoils produced by elastic scattering. Neutrons at energies above 1 MeV may produce recoils which interfere with the pulse-height spectrum because of ^{3}He (n,p) reactions. In fact, the cross section favors elastic scattering at neutron energies above 1.5 MeV. Pulse-shape discrimination is used here to suppress analysis of recoil events. However, our experience has shown that the risetime distribution of ^{3}He recoils is narrow and only slightly separated from that due to (n,p) reactions. Consequently, the effectiveness of pulse-shape discrimination in rejecting recoil events is very sensitive to minor distortions in pulse shape due to electronics effects.

The proportional counter system now in use consists of a "fast leg" where pulse-shape analysis is done on the output of a fast amplifier, and a "linear leg" where the pulse output is shaped for best pulse-height resolution. Even so, the reliability of measurements made with ^{3}He proportional counters has been somewhat disappointing. Whenever a large rejection ratio (in the range 20-30) is required for ^{3}He recoils, i.e. when the neutron differential flux above 1 MeV is not small compared to that at 0.5 MeV, a substantial penalty is paid in neutron detection efficiency since many (n,p) events are also rejected. Loss of 50% or more is not uncommon. More importantly, the reproducibility of the detector response is poor under these conditions because of minor variations in pulse shape at the discriminator between one setup and another. Variations of ±40% in the (n,p) detection efficiency have been observed among experimental setups which were intended to be the same. However, when lower rejection ratios (in the range 2-5) are acceptable, the ^{3}He proportional counters yield reproducible measurements of high resolution (25 keV at low energies to 75 keV at 1 MeV).

Conclusion. Laboratory neutron spectrum measurements are being made in the energy range 10 keV – 20 MeV at flux levels of 1 n/cm^2 sec to 3×10^4 n/cm^2 sec. Scintillators and hydrogen proportional counters have proven reliable and relatively easy to use while ^{3}He proportional counters must be used with some caution when measuring continuous spectra. The system described here is designed for use in a laboratory environment while an adaptation of it, described elsewhere in this report,[16] may be used in the field.

Development of a High-Resolution Neutron Spectrometer for Field Use

Many dosimeters used to measure personnel neutron exposures do not have a "rem response." Consequently, it is necessary to estimate the neutron energy spectrum in the work environment where these dosimeters are worn in order to infer the accumulated neutron exposure from the dosimeter response. A spectrometer system has been developed at LLL which may be transported to various work environments where dosimeters are worn or to locations where environmental radiation measurements are made. The system described here represents the adaptation for *field use* of the Laboratory Neutron Spectrometer System whose development has been chronicled in a series of earlier progress reports.[18-22]

System Configuration. The primary objectives sought in the development of a field neutron spectrometer system were:

- Reliability.
- Transportability, i.e. mass less than 100 kg.
- High sensitivity, i.e. useful at dose rates 1-100 mR/hr.
- Wide energy range, i.e. 10 keV – 20 MeV range.

To obtain a system meeting the requirements of field use, some sacrifices have been made in performance. Pulse-shape discrimination has been used in laboratory measurements to suppress the gamma-ray response of hydrogen proportional counters, but no shape discrimination is used with proportional counters in the field system. Instead, a lead cover 6 mm thick is placed over the proportional counters. This introduces some distortion of the neutron spectrum (up to 10% of the differential flux), but the gamma-ray response is reduced by a factor of 2-10. Even so, the gamma-ray response often causes greater contamination of the pulse-height spectrum than a bare detector used with pulse-shape discrimination. A secondary benefit of the lead, however, is a substantial reduction of the detector response to acoustic noise and mechanical vibration which have been important in some field measurements.

The electronics configuration used is shown in Fig. 15. The system in use is shown in Fig. 16. At the right of the photograph is a Nim-bin containing the electronics. Also shown is a portable oscilloscope used in the system setup. At the left is the LLL "computing gamma-ray spectrometer" which is used here as a portable pulse-height analyzer.

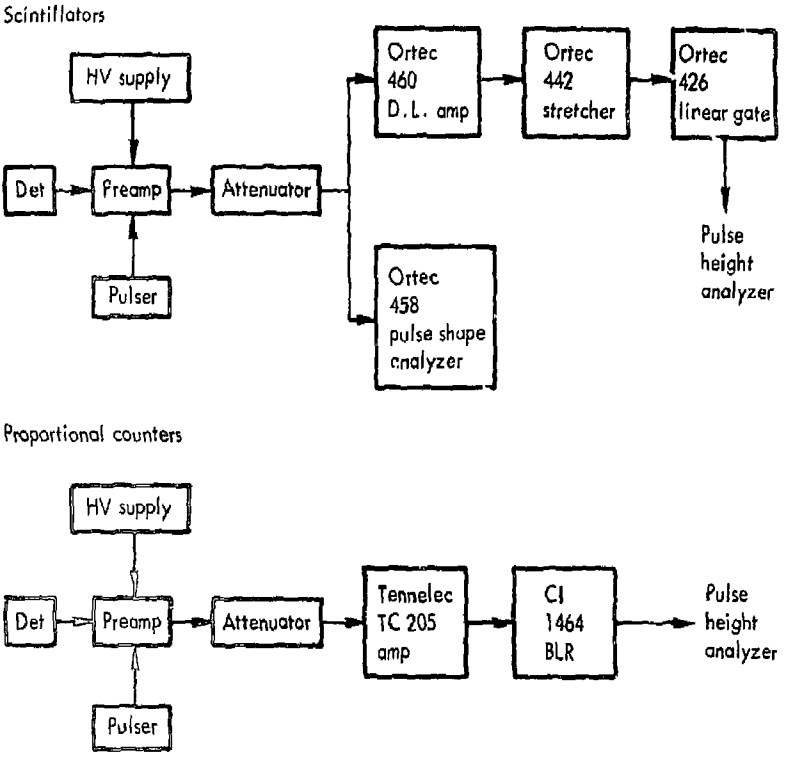

Fig. 15. Electronics configuration for scintillators and proportional counters in Neutron Spectrometer Field System.

In addition to the electronics package, the spectrometer includes a suitcase containing an array of neutron detectors. The array is shown in Fig. 17. On the lower portion is a large NE 213 liquid scintillator (front) and one of two hydrogen proportional counters. The top portion contains three additional NE 213 scintillators as well as a ^{3}He proportional counter and a small hydrogen proportional counter.

Total masses of the system components are:

• Electronics	42 kg
• Pulse-height analyzer	18 kg
• Detector array and suitcase	18 kg
Total	78 kg

Operating Experience. Energy calibration of the NE 213 scintillators in the field is accomplished using a ^{22}Na gamma-ray source. Compton edges in the pulse-height spectrum due to 0.511- and 1.28-MeV gamma rays are located, and the data of Verbinski[23] (relating light output from recoil protons to that of Compton electrons) is used to relate proton energy to the pulse height at which the Compton edges occur. Calibration of the proportional counters may sometimes be accomplished on the basis of thermal neutron interactions with N_2 which constitutes 5% of the gas mixture. The resulting (n,p) reaction produces pulse-height response equivalent to that from a 0.615-MeV proton.[24] A linear pulser is then used to locate the zero energy point. In the absence of a suitable source of thermal neutrons, measured characteristic curves of gas multiplication versus anode voltage are used to infer proton energy from the charge collected in the detector. Some of these curves are given elsewhere in this report.[17]

Neutron spectrum measurements have been made at the Nevada Test Site and at the LLL site boundary. In both cases, the system appeared to be reliable and reasonably convenient to transport. There is not yet enough data to assess the accuracy of measurements made in the field, but an intercomparison is being planned to compare results obtained using the field

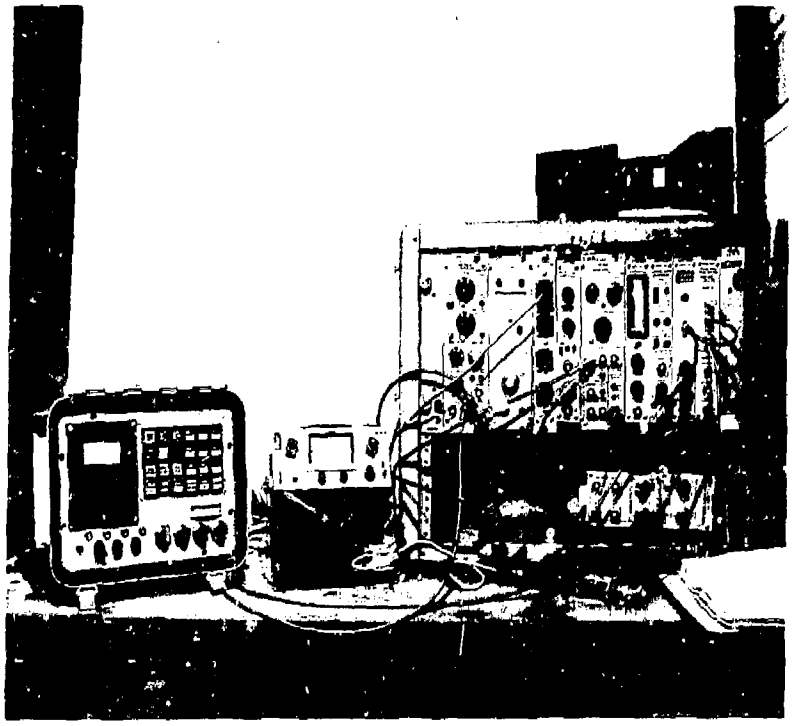

Fig. 16. Neutron spectrometer system.

system to those obtained from: (1) calculations, (2) laboratory measurements, (3) bonner sphere measurements.

Fig. 17. Neutron detectors.

Capabilities. The sensitivity of the various detectors used depends on their active volume and density of hydrogen or ^{3}He. Consequently, several specimens of each detector type are available for spectrum measurements. Table 4 contains a list of the detectors, together with their nominal energy resolution and the range of neutron intensities over which each detector is useful.

Generally, the resolution of the system is 5-10%. Sensitivity at energies above 1 MeV is adequate for measurements where the neutron exposure rate is larger than 0.1 mR/hr with a maximum field on the order of 3 R/hr. The sensitivity at lower energies is less. Spectra have been measured down to 50 keV in fields as low as 1 mR/hr, but the counts must be long and the statistics are not often good. Measurements have been made routinely in the energy range 100 keV 20 MeV. Some spectra have been obtained down to 10 keV in low gamma-ray environments.

Conclusion. Extension of the useful energy range of proportional counters to low energies may only be obtained with sophisticated pulse-shape discrimination

Table 4. Detector parameters for field neutron spectrometer

Detector description	Useful energy range (MeV)	Energy resolution	Useful neutron intensity range (n/cm^2 sec)	
NE 213 liquid scintillator 5.08 x 11.4 cm diam	1-20	7%	1 - 100	at 3 MeV
NE 213 liquid scintillator 7.6 x 3.8 cm diam	1-20	7%	10^1 - 10^3	
NE 213 liquid scintillator 2.5 x 2.5 cm diam	1-20	7%	4×10^1 - 3×10^3	
NE 213 liquid scintillator 1.3 x 1.3 cm diam	1-20	7%	3×10^2 - 3×10^4	
H_2 proportional counter 20 atm, 45.7 x 5.08 cm diam	0.3-3.0	7%	10^1 - 10^3	at 0.5 MeV
H_2 proportional counter 3 atm, 25.4 x 3.8 cm diam	0.03-1.0	5%	2×10^2 - 2×10^4	
H_2 proportional counter 1 atm, 45.7 x 5.08 cm diam	0.01-0.3	?	2×10^2 - 2×10^4	
He^3 proportional counter 4 atm He^3, 4 atm Ar, 45.7 x 5.8 cm diam	0.2-2.0	40-100 keV	5×10^2 - 5×10^4	

techniques and reduction of gas pressure and volume. Such extensions reduce the system sensitivity and increase its complexity substantially. The system described here is adequate for data acquisition under the conditions stated, but does not now offer any real-time capability for data interpretation. Neutron spectra are obtained only after reduction of the pulse-height data on a large computer. Some effort is now being expended to provide a data display which would lend itself to at least a crude visual interpretation by an experienced operator of the system. Additional effort is being expended to assess the accuracy of the spectra obtained with the field system.

Modified Chlorine and Hydrogen Chloride Cartridge Testing System

The chlorine and hydrogen chloride cartridge testing system measures the effective cartridge and canister life under the conditions set forth in Title 30 CFR Part 11.

A cartridge is subjected to test concentrations of 0.05, 0.5, or 2.0% at 32 or 64 litres/min. The relative humidity is set at 50%. An analyzer is placed downstream and the effluent concentration is monitored as a function of time. Upstream and downstream temperatures are measured continuously throughout the test.

A generalized block diagram of the system is shown in Fig. 18. Laboratory compressed air is humidified and blended with chlorine or hydrogen chloride in the gas flow control module. The humidifier is continuously supplied with water and regulated with a humidity controller. During initial start-up, the gas mixture passes through a bypass while the cartridge to be tested is placed in the cartridge holder.

The testing period is initiated by switching the gas flow from the bypass canister to the test cartridge. An analyzer continuously monitors the effluent concentration and displays the results on a recorder. The apparatus is shown in Fig. 19.

The gas flow control module is shown in Fig. 20. This unit activates the air, chlorine, hydrogen chloride, and water supplies; controls the gas flows; provides power for the relative humidity controller; measures the temperature; and switches the gas flow from the bypass canister to the cartridge under test.

When in the normal testing mode, air is humidified by activating the heater in the water reservoir. The humidity is measured with a solid-state sensor. The air flow is adjusted and measured with the flowmeter and then merged with a predetermined flow of chlorine or hydrogen chloride in a mixing chamber. The gas mixture then passes either out the bypass canister or to the test cartridges. A digital temperature gauge monitors the inlet and outlet cartridge gas temperatures.

This apparatus was built for the Testing and Certification Laboratory under reimbursable contract NIOSH-1A-74-21, and this system concludes our work for the National Institute of Occupational Safety and Health.

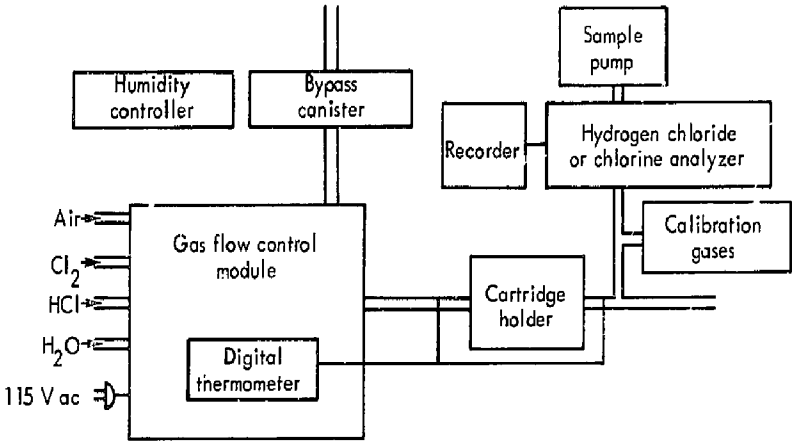

Fig. 18. Block diagram of the chlorine and hydrogen chloride cartridge testing system.

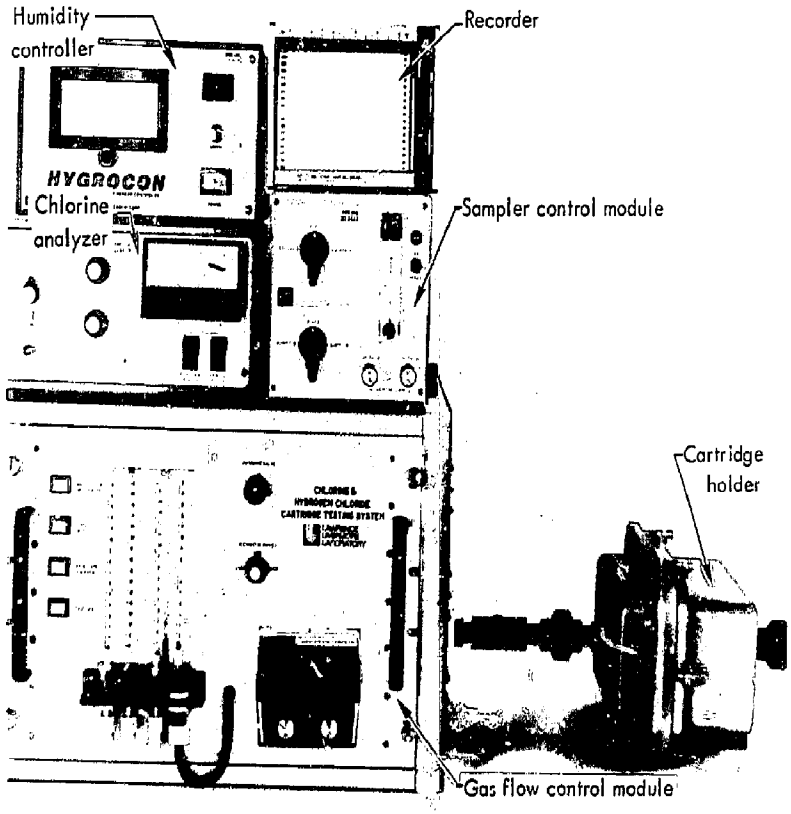

Fig. 19. Modified chlorine and hydrogen chloride cartridge and canister testing system.

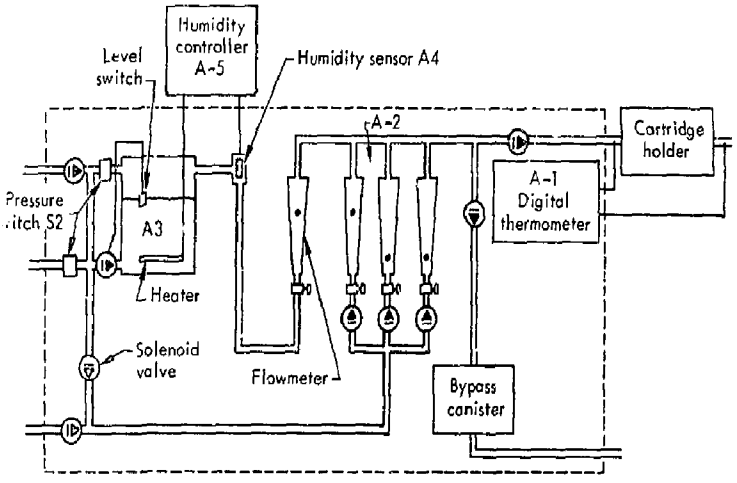

Fig. 20. Schematic diagram of gas flow control module.

A Portable Gamma Spectrometer

Due to needs of Hot Spot emergency response and general health physics monitoring, Hazards Control has been funding a project to build a rugged, truly portable, gamma spectrometer. A first unit has been built which has been designated LEA74-1040 (Fig. 21) The instrument has been in use and has been upgraded many times as new circuitry is designed to improve performance. Typical uses to date have been monitoring of neutrons near the linear accelerator; measurement of ^{239}Pu samples in the chest of a cadaver for calibration purposes of the Whole Body Counting Facility; and measurement of nuclear devices at NTS. The instrument has also been borrowed for use off-site on many spur-of-the-moment occasions to measure the isotopic composition of an unknown sample.

The prototype analyzer was completed in October 1974 after which time we decided not to build more of that design but to work on a second-generation machine which would more adequately suit the needs of various users and solve some of the stability and maintenance problems that were present in the first analyzer. Some of the specifications of the new analyzer will be discussed at the end of this report.

The present analyzer consists of an aluminum watertight container 204 X 280 X 560 mm in size, and has a weight of 19 kg. The instrument contains a 256-channel pulse-height analyzer with computing capabilities, a combination light-emitting diode (LED) and cathode-ray tube (CRT) display, a Polaroid camera housed in the cover, a 50- X 50-mm NaI(Tl) detector housed in a side well, and a 1-kV power supply for the detector. The cover also contains a folding 1-metre tripod for using the detector outside the instrument if desired (Fig. 22). A line cord for charging the instrument's Gel-cell batteries, plus extra cables and film, are also included in the cover. A waterproof side door covers the detector well, a.c. charging receptacle, and the time-setting switches for the time-of-day clock.

The analyzer was designed to be reliable in the environment of a Hot Spot accident anywhere in the world. A temperature range of -30 to +70°C will not affect correct operation of the instrument, but small calibration changes might be necessary if one transfers the instrument from room temperature to -30°C arctic climate. Changes are presently being made to allow no-drift performance over the full range, making the NaI detector the only weak link.

The analyzer is designed to be submersible with its cover closed, and is splashproof with the control panel exposed. Salt spray environments were not considered on the first unit, but will be included in the design consideration on the new analyzer which has a fiberglass case and is made of special construction materials. The fiberglass case will also give better resistance to shock and denting than the aluminum case does.

The analyzer was intended for use in situations where an operator might need to wear gloves, and thus we designed the controls to be almost exclusively pushbuttons. A special tool is enclosed in the cover for use as a button pusher or adjustment tool. Keyboard buttons also are quicker and most of the

Fig. 21. Front panel view of the prototype analyzer shows operating keyboard and combination CRT and LED display. The graticule is not illuminated and does not show well here.

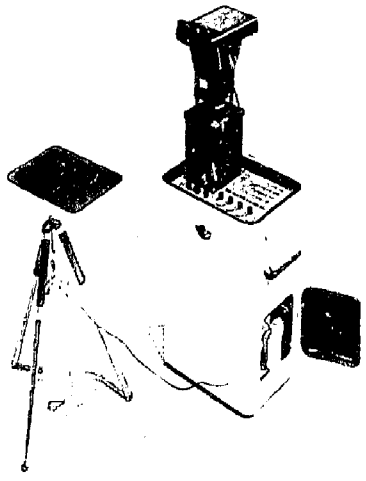

Fig. 22. The portable analyzer may be used with its integral NaI (TL) detector removed and hung on the expandable tripod which is housed in the instrument cover.

time easier to use than other types of switches. Twenty-four pushbutton switches are used, some of which have a double function.

Special features that were incorporated into the analyzer are as follows:

- 40-character LED display adjacent to CRT so that all pertinent information is photographed to prevent needless writing on the back of photos (Fig. 23).
- Internal time-of-day plus day-of-year clocks provide correct time on the display, along with other LED data and the CRT plot for photo purposes.
- Two movable markers one reads out in counts and energy in keV.

- Live instead of twinkle display on CRT. May be used during acquiring of data as desired, or may be shut off to conserve power.
- Battery life 10 to 20 hours depending on use; recharges in 8 hours. Needs no connection to any other equipment. Will operate with covers closed for severe climates.
- Automatic photo exposure controlled by the analyzer.
- Digital direct-energy readout which can be set up to 4076 keV full-scale in 1024 increments.
- Two modes of integration: one $\sum_{A}^{B}$, another $\sum_{A}^{B}$-background where background is approximated as the straight line drawn between points A and B.
- Two-digit sample number for record keeping. Number appears in LED display.
- Digital scale factor push-button control for CRT allows quick change of CRT from 100 counts full-scale to 100 k counts full-scale in 29 increments.
- Maximum preset live-time of 99999 seconds. May be changed while analyzer is acquiring data. Will stop if number is entered which is less than the present live-time.
- CRT has horizontal magnification and position controls to allow viewing a small portion of the CRT trace.
- Lightweight Polaroid camera uses type-87 film which does not need coating.

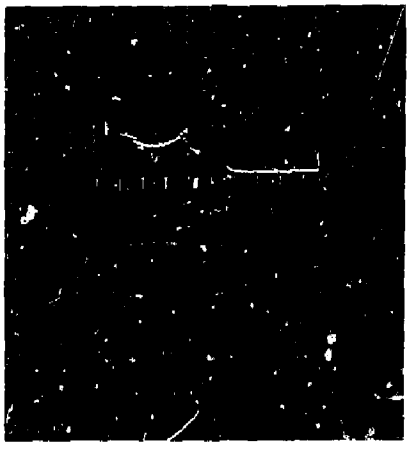

Fig. 23. A polaroid photograph is easily produced by the instrument and its self contained camera. Time of day + day of year automatically appear in the display for record keeping.

Fig. 24. Looking into the instrument case with front panel removed shows a crowded array of components. Batteries + high voltage supply are behind the detector well (black tube). Logic board containing 300 ICS is at lower portion of photo.

The interior of the analyzer is constructed of approximately 300 CMOS integrated circuits on a foldup wirewrap frame plus about four other printed circuit boards containing another 100 CMOS circuits for the analog-to-digital converter, display drivers, and time-of-day clock (Fig. 24).

The analog-to-digital converter is a conventional Wilkinson type with linear rundown of a capacitor. The circuit is special only in its power consumption, concern for temperature drift, and speed (4 MHz for 256 channels).

The amplifiers and preamplifier consists of two type AD 507 operational amplifiers in a charge-sensitive design. Maximum sensitivity is 0.5 picoCoulombs full scale. The memory is all CMOS consisting of 20 RCA CD4061 256 X 1 memory chips. The meory is arranged as 20-bit BCD words to allow a maximum channel capacity of 100 000 counts.

The CRT is made by Tektronix for their Model 211 Oscilloscope. The driver amplifiers were also used from the same oscilloscope. The LED's are multiplexed at 20 kHz to provide a no-flicker display.

User Experience. During use by many persons in the field, including the author on demonstration trips, some features worked out to be very useful; however, problems did arise. The keyboard operation worked out very well, allowing a new user to be acquiring data in a few minutes once he read the small enclosed plastic instruction card. It has been very useful to have

a self-contained system where the user need not be knowledgable in electronics to use the device. The multiple LED display allows the user to know immediately what the result of button pushing is even if he is not sure of its function. The direct readout in keV (channel numbers may also be used) allows easy determination of most isotopes. Problems, arise, however, from the non-linear characteristic of NaI(Tl) detectors below 400 keV. A keV offset must be added to the curve to allow linear readout over a small range. The present analyzer is offset in the ADC to do this. Several spectra need to be run to calibrate, which wastes time. The second design presently under construction will simplify this procedure by providing digital offset. Also, the new analyzer will use more integrated circuits in its ADC to make a more stable converter with respect to temperature and battery fluctuations.

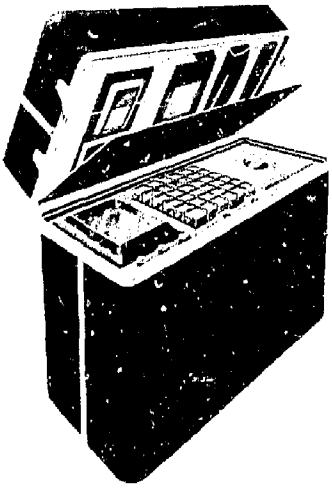

Fig. 25. *An artist's conception of the new model under* design shows 8 × 70 display camera in cover and more ruggedized fiberglass case.

Features for the Second-Generation Analyzer. Many design changes are being made in the new analyzer (Fig. 25) now being constructed. The more important of these are as follows:

- 1024- or 256-channel operation
- Four groups of 256 channels may be moved, added, or subtracted from each other.
- ADC clock rate is 8 MHz.
- External ultra-pure Ge detectors may be used.
- Log or linear display.
- New energy multiplier circuit of the form Energy of channel = (channel #)(keV/channel const) + keV offset.
- SX70 Polaroid camera, to photograph CRT and LED's; fully automatic operation produces ten photos in 20 sec if desired.
- Accessory data tape recorder may be used – Sony TC 55 is adequate (audio tape recorder).
- FSK telemetered data output may also be used to send data over phone with accessory phone coupler.
- Analyzer will stop on preset live-time, on preset count in a specific channel, or on overflow in any channel.
- Amplifier gain is digitally controlled in seven binary steps from the keyboard.
- NaI detector provided is rugged and protected against temperature changes.
- Fiberglass case is waterproof and drop-proof.
- Analyzer will meet military transportation specifications.

FIRE SAFETY

HEPA-Filter Fire Protection

In our previous report we detailed the results of attempts to scrub smoke particulates from an air stream using a fine water spray containing a Teflon additive and a rolling prefilter consisting of cheesecloth backed by a flyscreen. We indicated that one experiment showed some promise in extending filter life, and that the results would be checked.

We modified the smoke generation system to eliminate soot buildup in the stack feeding the main air duct and made other adjustments to ensure close control of the test operation. Following this, we conducted several tests in an effort to duplicate the previously reported promising single result. These efforts have all been unsuccessful, as can be seen from the data in Table 5, and the typical air-time and pressure-drop-time curves shown in Fig. 26. We have therefore stopped this effort, and testing will resume after activation of the full scale fire test cell.

During the past several months construction has progressed on the large-scale fire test cell and auxiliary facilities, and completion is expected about July 15,

Table 5. HEPA filter smoke plugging ts, using rolling prefilter and warm (~150°C) smoke

Run No.	Avg. life (min)	ΔP_3 prefilter (Pa) Initial	Final	ΔP_4 HEPA (Pa) Initial	Final	Duct air flow (ℓ/sec) Initial	Final	Runtime (Min)	Remarks
30	24-31	7	1244	249	1717	455	342	160	Test of spray w/additive on rolling prefilter.
31	0	0	0	299	2289	455	257	125	No prefilter; test of spray effect w/o prefilter
32	0	0	0	239	1941	460	250	100	No prefilter, no spray. Baseline plugging-time test.
33	1-25	5	30	398	1916	444	253	105	Attempts to duplicate Run 30, but with better control of operating conditions, e.g., fuel- and water-feed.
34	.8-34	7	72	299	1966	460	253	100	
35	9-29	5	995	274	1841	463	253	100	
36	11-19	10	498	299	1269	477	316	85	

Conditions:
1. Fuel – neoprene hypalon gloves
2. Fuel feed – 100 g/min
3. Prefilter – 1 layer cheesecloth with screen wire backing
4. 0.12% Teflon in water
5. 0.01-ℓ/s water spray

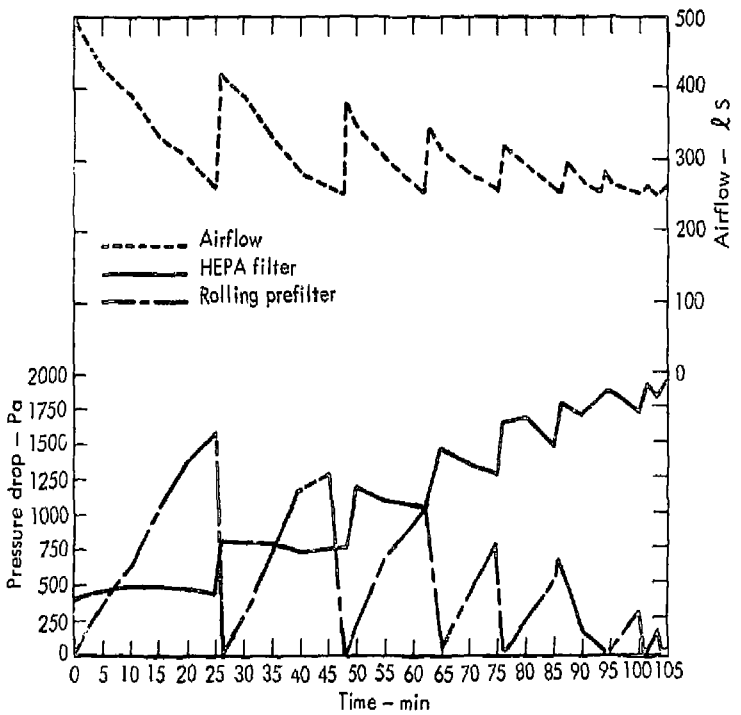

Fig. 26. HEPA filter smoke plugging test – airflow through duct and pressure drops across prefilter and filter.

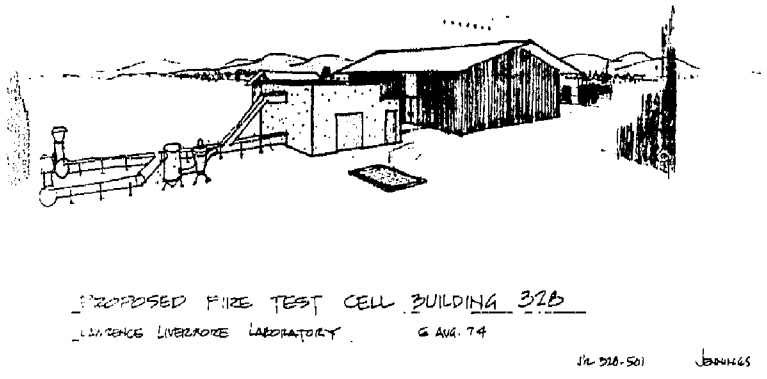

Fig. 27. Proposed fire test cell – Building 328.

1975. Activation – including addition of the ductwork and air pollution control system and installation of the 100-channel computerized data acquisition system – will take approximately three months. An architect's rendering of the cell and associated ductwork is shown in Fig. 27. Interior dimensions of the cell are 5.94 X 3.99 X 4.22(H) metres with an enclosed volume of 100 m^3. Some 32 possible experiments are planned as combinations of the following:

- Four fuel loadings
- Two sprinkler conditions (on-off)
- Two ignition sources (inside/outside an enclosure, e.g., a hood or gloved box)
- Two exhaust locations (high/low)

Concerning the fuel loadings, these will consist of surplus ERDA-contractor laboratory items (gloved boxes, hoods, benches, tables, supplies, etc.) arranged in realistic arrays.

The fuel loadings selected are shown in Fig. 28, plotted as D/C (dirty-to-clean ratios) versus combustible loading in kg/m^2 of floor area. These were arrived at under the following considerations.

- With the cooperation of various ERDA-contractor representatives, lists of equipment and photographs were obtained for various typical laboratory and processing installations.
- From this information tables were prepared of combustible floor loadings, and dirty-to-clean (smoke) ratios of the materials, equipment and products involved. A dirty smoker is defined as a material which in a well ventilated fire, produces (based on our experience) copious quantities of smoke particulates; a clean smoker is the opposite. Dirty smokers include certain plastics and cellulosics, particularly those which are fire-retarded. Clean smokers include most cellulosics and some plastics.

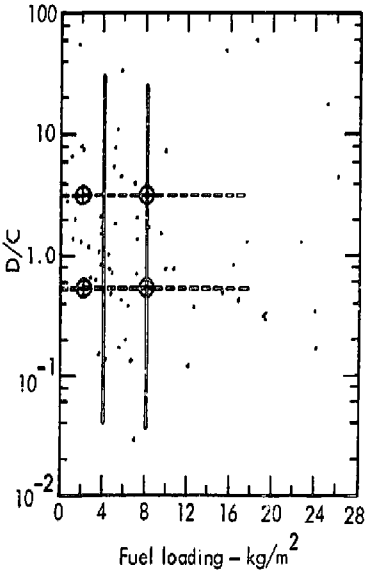

Fig. 28. Fuel loading of sample labs as dirty-to-clean ratio.

- From the tabulated data, the plot was prepared and a quasi-mathematical analysis of the groupings of the various points was made. From this, four values were selected: D/C 0.5 and 3; and fuel loadings 8 and 2 kg/m^2, respectively. (These are the values marked with the ⊗ on Fig. 28.

In the planned experimental program, laboratory equipment and materials will be set up to simulate these smoke/fuel loadings as closely as possible.

Smoke-Chamber Results on ASTM Round Robin

Recently, we participated in a round robin test sponsored by ASTM (American Society for Testing and Materials) in which some 30 laboratories were to test 23 materials and products in the NBS Smoke Density Chamber under both nonflaming and flaming exposures. The purpose of this round robin was to determine replication within a laboratory and duplicability among laboratories. Procedures were standardized; these were a modification of that given in NBS Technical Note 708.

The materials and products tested are shown in Table 6. Our average results are shown in Table 7. Our replication was generally quite good. Also shown in Table 7 are our results for maximum concentrations of CO (carbon monoxide) and CO_2 (carbon dioxide), obtained by sampling the chamber atmospheres during the third test of each exposure condition for each kind of material.

Sampling and Analytical Procedures. For each gas, sampling was continuous at the rate of 500 ml/min drawn from the top center of the chamber by means of a vacuum system. Fresh air (total 1000 ml/min) was admitted to the bottom of the chamber near the back. (For the 20 min of test time involved, this amounted to about 0.1 chamber air changes per hour. This ventilation rate seemed to have no effect on the smoke density values obtained.) The samples were passed through particulate filters – and in the case of the sample to be analyzed for CO through a presaturated carbon filter – and then respectively through individual nondispersive infrared spectrometers. Each spectrometer was frequently calibrated using cylinder gases of known concentration. In turn, these cylinder gases were calibrated by means of a mass spectrometer.

Values for CO and CO_2 were read and recorded every 5 min during the test.

Results and Discussion. The smoke density values, i.e. maximum specific optical density and obscuration time (T-16), are quite like those we have reported previously for similar materials.[25-27] They will not be discussed further.

Table 6. Materials tested

		Sample thickness (mm)
1.	Hardboard, unfinished	6.4
2.	Particle board, untreated	9.5
3.	Lauan hardwood plywood unfinished, A-D	6.4
4.	Hemlock, untreated	19.1
5.	Hemlock, treated	19.1
6.	Red oak	19.1
7.	Acoustical ceiling tile	12.7
8.	Nonacoustical ceiling tile, untreated	12.7
9.	Standard gypsum board	12.7
10.	0.8-mm high-pressure standard decorative laminate, urea glue on 19.1-mm untreated particle board	19.9
11.	0.8-mm fire-retarded high-pressure decorative laminate resorcinol adhesive, on 19.1-mm treated particle board	19.9
12.	Linoleum	3.2
13.	Wool plush carpet	~12.7
14.	Polyester twist carpet	~12.7
15.	Nylon twist carpet	~15.9
16.	Acrylic carpet	~8.0
17.	Fiberglass-reinforced brominated polyester sheet	2.5
18.	Polyvinyl chlorine flooring	3.2
19.	Polystyrene sheet	3.2
20.	Polymethylmethacrylate sheet	3.2
21.	Fiberglass-reinforced polyester sheet	2.5
22.	Flexible urethane foam, high resiliency	12.7
23.	Rigid polyisocyanurate foam	12.7

Concerning the results for CO_2, we have recently determined, using blank asbestos-cement board specimens, that this gas is not present in detectable quantities under the nonflaming exposure. However, under the flaming condition, the pilot gas flame accounts for a concentration of about 1.4% in 20-30 min of test time. Hence, the values reported in Table 7 should probably be reduced by this amount.

In regard to carbon monoxide concentrations, we have segregated the materials into various groupings, less than 500 ppm, 500-1000 ppm, etc., as shown in

Table 8, in an effort to categorize them if possible. Inspection of this table shows that gypsum board and the particular urethane foam yield less than 500 ppm of CO under either exposure. This can be explained on the basis of the small amount of heat-degradable materials involved, and the easy access of oxygen (in air) to the degraded species.

At the other end of the spectrum, red oak, untreated hemlock, and both kinds of ceiling tile all yield in excess of 2000 ppm under either exposure. Under the nonflaming condition, the thickness of the red oak and untreated hemlock and the compaction of the hardboard and particle board, suggest that that incomplete combustion is occurring within the sample, thus leading to this high production of CO. The same may hold true for the red oak, untreated hemlock and hardwood plywood, under the flaming exposure.

The high production of CO from the ceiling tile samples may be attributed to the immediate charring of the surface coating; this may have tended to seal the base material so that oxidative degradation or combustion occurred in a limited oxygen supply.

Concerning the treated hemlock and brominated polyester under flaming exposure, fire retardants are suspected of interfering with the combustion process. Hence, one would expect that combustion of these kinds of materials would be such as to produce significant quantities of carbon monoxide.

Table 7. Specific smoke chamber results obtained on ASTM round robin materials[a]

	Exposure condition							
	Nonflaming				Flaming			
			Maximum				Maximum	
Material	D_{mc}	t_{-16}	CO	CO_2	D_{mc}	t_{16}	CO	CO_2
Hardboard	519	3.0	2650[b]	0.8[b]	94	5.1	1300	4.2
Particle board	522	2.6	3500	0.9	138	6.9	1400	4.2
Hardwood plywood	372	2.8	850	0.7	76	5.7	2500	2.9
Hemlock, untreated	521	3.1	2650	0.9	481	3.1	2750	3.3
Hemlock, treated	85	4.5	800	-0-	101	1.7	2500	1.7
Red oak	524	3.5	2500	0.4	185	7.3	2500	4.4
Ceiling Tile, acoustical	318	1.5	4500	0.8	146	4.3	2500	2.4
Ceiling Tile, non-acoustical	244	1.2	4750	0.8	126	4.4	2750	2.3
Gypsum board	54	3.2	300	0.1	20	3.0	300	0.9
Standard decorative laminate	453	2.7	1500	0.7	315	1.9	1850	3.3
Fire-retarded decorative laminate	169	2.6	500	0.2	260	1.1	1900	1.4
Linoleum	515	1.9	700	0.6	390	1.2	550	2.9
Wool plush carpet	452	0.9	100[b]	0.2[b]	497	1.3	1050	2.1
Polyester twist carpet	413	2.9	1100	0.2	253	1.7	900	2.2
Nylon twist carpet	247	1.4	350	0.3	307	0.8	700	2.3
Acrylic carpet	326	1.3	450	0.2	262	0.8	510	2.0
Brominated polyester sheet	522	2.3	350	-0-	467	0.8	2700	1.9
PVC flooring	282	2.3	100	0.2	297	1.2	1500	1.8
Polystyrene sheet	403	3.0	150	0	526	0.8	1100	4.0
Polymethylmethacrylate sheet	66	5.7	240	0	208	1.4	650	5.5
Fiberglass polyester sheet	457	2.8	250	0.1	346	0.8	900	3.3
Polyurethane foam	83	0.8	0	0	98	0.4	500	0.9
Polyisocyanurate foam	24	0.7	380	0	41	0.4	650	1.1

[a] D_{mc} = maximum specific optical density, corrected for soot on optical system
t-16 = time (min) to reach Ds = 16 (Ds = spec optical density)
CO values are in parts per million (ppm)
CO_2 values are in percent by volume

[b] At 15 min of exposure time; all other CO/CO_2 concentrations were obtained at 20 min of exposure time.

Table 8. Analysis of maximum carbon monoxide concentrations in smoke chamber obtained on ASTM round robin materials

Maximum CO (ppm)	Nonflaming	Flaming
< 500	Gypsum board Polyurethane foam Fire-retarded decorative laminate Fiberglass polyester sheet Polymethylmethacrylate sheet Polystyrene sheet Brominated polyester sheet Polyvinyl chloride flooring Polyisocyanurate foam Acrylic carpet Nylon twist carpet Wool plush carpet	Gypsum board Polyurethane foam
500 – 1000	Hardwood plywood Hemlock, treated Linoleum	Nylon twist carpet Polyester twist carpet Linoleum Acrylic carpet Polyisocyanurate foam Fiberglass polyester sheet Polymethlymethacrylate sheet
1000 – 2000	Standard decorative laminate Polyester twist carpet	Standard decorative laminate Fire-retarded decorative laminate Hardboard Particle board Polystyrene sheet Polyvinyl chloride flooring Wool plush carpet
> 2000	Red oak Hemlock, untreated Ceiling tile, acoustical Ceiling tile, non-acoustical Hardboard Particle board	Red oak Hemlock, untreated Ceiling tile, acoustical Ceiling tile, non-acoustical Hardwood plywood Hemlock, treated Brominated polyester sheet

DECONTAMINATION

Enhanced Filtration

For the past year, the Special Projects Division has been working on a reimbursable contract for the Division of Waste Management and Transportation (DWMT) to extend the life of high-efficiency particulate air (HEPA) filters. These filters remove airborne particulate matter from a number of radioactive materials handling facilities. If filter life could be increased, the following benefits would be realized:

- Less handling of contaminated filters.
- Reduction of bulk of radioactive waste to be processed and buried.
- Reduction of number of filters required.

We have considered several approaches which may extend the HEPA filter service life. More efficient prefiltering materials or techniques could be developed. Also, particles could be coalesced into larger particles and hence could be collected more efficiently by either the HEPA or prefilter. For our initial experiments we have chosen the latter technique, and will attempt to coagulate particles using electronic charging techniques.

Experimental Design. Figure 29 shows a schematic of the HEPA filter testing apparatus. Basically the system consists of an air mover, aerosol generator, aerosol modification section, filter holder and service life diagnostic equipment.

A 1500-cfm (700-litre/sec) capacity blower moves air through the ductwork assembly. The flow (usually 235 litre/sec) can be varied using the adjustable dampers at the system inlet and outlet.

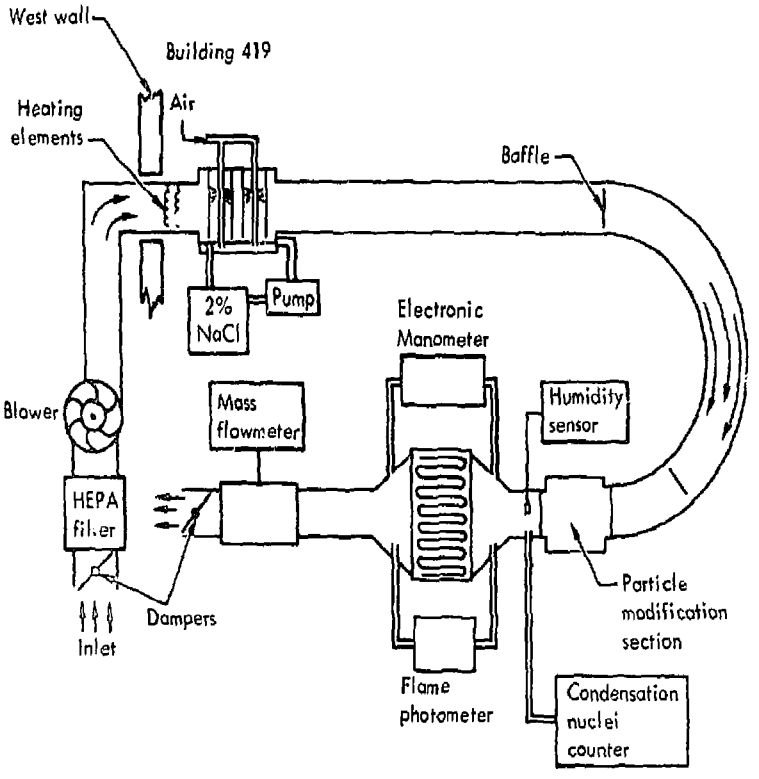

Fig. 29. Schematic diagram of HEPA-filter service life measurement system.

A sodium chloride test aerosol is generated by aspirating a 2% salt solution into four atomizers using compressed air. The resultant droplets dry as they move down the duct and a solid, polydispersed aerosol is formed. Heaters are sometimes required to aid in the drying process, and baffles are provided for proper mixing. A recirculation pump provides a continuous flow of solution into the spray box.

The aerosol then passes into the particle modification section where it undergoes coagulation or prefiltration. A condensation nuclei counter continuously monitors the particle number concentration. The aerosol then passes through the filter under test, through a mass flowmeter, and is exhausted outside the building.

Filter service life diagnostic equipment includes an electronic differential pressure manometer which monitors pressure drop as a function of time, and a flame photometric sodium detector to measure filter efficiency. Relative humidity, airflow and temperature are also recorded throughout the testing period.

Preliminary Results. The particle modification system is not yet quite complete. We have run three filters to determine what the loading characteristics are with no prefilter or particle agglomeration. These data

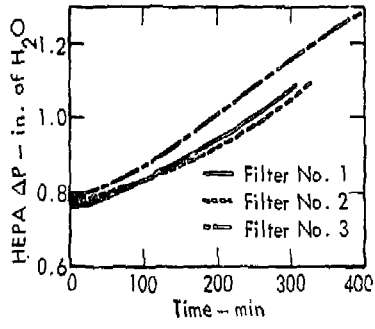

Fig. 30. Pressure drop as a function of time for 3 to 500-cfm HEPA filters.

are shown in Fig. 30. Note that the pressure drop growth rate (slope) is about the same, but is displaced slightly due to small differences in filter construction.

We conducted these tests with 235-litre/sec capacity filters which exhibited efficiencies greater than 99.95%. The salt concentration was approximately 10 μg/litre. This represents a filter loading of about 250 $\mu g/sec/m^2$ of filter surface.

Technical Notes

RADIATION PROTECTION

An Unusual Problem in Tritium Dosimetry: Tritium in Glass

Glass microballoons having a diameter in the range of 30 to 100 μm and a wall thickness of about 7 μm are used at this Laboratory as targets for laser fusion experiments. The microballoons are filled with a deuterium-tritium gas mixture by diffusing the gas through the wall at high temperature and pressure. A typical microballoon will contain several microcuries of tritium after loading.

Preliminary hazards analysis indicates that these microballoons will present little hazard so long as they remain intact. If a microballoon is broken, a slight hazard will exist for a short time due to the release of the contained tritium. However, a long-term respiratory hazard may exist because of tritium contained in the glass fragments of a broken microballoon.

We have examined the fragments of a number of broken microballoons, and many are in the respirable size range. Further, we have confirmed that some tritium is trapped in these glass fragments and retained for long time periods. Work is underway to determine the following:

- The particle size distribution of the glass fragments from broken microballoons.
- The quantity of tritium contained in the fragments and its rate of diffusion from the glass into the air.
- The rate dissolution of the glass fragments (and, hence, tritium) in the lung as determined by the rate of dissolution in simulated lung fluid at body temperature.

With these data, we will be able to calculate the hazard involved in handling the microballoons. However, a preliminary estimate of relative hazard can be made by assuming the inhaled glass fragments are essentially insoluble (ICRP Class Y) in the lung and are eliminated with a half-life of about 1 year. If this is the case, an incident that deposits 100 μCi of tritium in this form in the pulmonary lung will deliver about 20 rad to the lung over the course of the several years required to eliminate the tritium. Contrasted with this, we find that 100 μCi of tritium inhaled as water will deliver a dose of only 0.007 rad to the lung (and whole body).

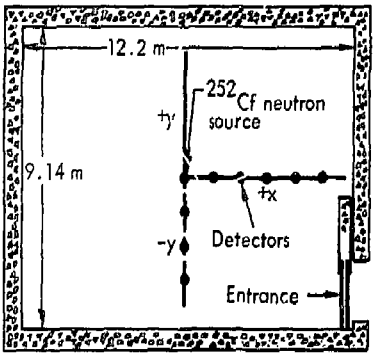

Fig. 31. Horizontal section depicts the shielding of low-scatter calibration cell and the locations of measuring points.

Fission-Neutron-Scattered Dose Contributions In the Low-Scatter Facility

The contribution of a scattered neutron dose to a total dose was estimated with the use of the Morse-L Monte Carlo Code[28] and the 30-group L-Division neutron library cross sections. Experimentally, the dose equivalent was measured with standard neutron rem counters, namely the Anderson-Braun and 22.86-cm-diam Cd-loaded polyethylene sphere rem counters. The results of this study indicate that the contribution made by the scattered neutron dose rate starts to become a significant part of the total dose rate as the detector and neutron source separation distance increases in the low-scatter cell. The majority of the contribution is from the neutrons scattered off the concrete shielding. It is therefore necessary to incorporate this scattered dose rate when calibrating the neutron rem counters.

The layout of the calibration facility and the corresponding detector locations are shown in Fig. 31. The cell is 12.2 m long, 9.14 m wide and 7.32 m from basement to ceiling. The concrete shielding walls and ceiling are 0.62 m thick. In Monte Carlo calculations, the basement floor of the cell (concrete and earth) was simulated with 0.62-m-thick concrete. The shielding door slab is 2.33 × 2.44 m and 0.46 m thick. The elemental compositions of concrete and air used in the calculations are given in Table 9.

The fast-fission neutron source was assumed to be point-isotropic, and was located in the center of the

calibration cell positioned 3.738 m above the basement floor.

Table 9. Material compositions

Material	Isotope	Atomic density (atom/barn-cm)
Air	O	1.001×10^{-5}
	N	4.076×10^{-5}
Concrete	H	1.386×10^{-2}
	C	1.200×10^{-3}
	O	4.582×10^{-2}
	Mg	1.100×10^{-4}
	Al	1.740×10^{-3}
	Si	1.063×10^{-2}
	Fe	3.500×10^{-4}
	Ca	1.520×10^{-3}

The calculated results are summarized in Table 10. The Monte Carlo statistical errors exclude the uncertainties in the library cross sections. The experimentally measured results for the ^{252}Cf neutron source are summarized in Table 11. In both tables, the dose-equivalent rates are normalized to a source strength of 1 n/sec. Dose conversions were made by using the values published in ICRP Publication 21.

Both the Anderson-Braun and 22.86-cm-diam sphere rem counters were calibrated against the Monte Carlo dose rate at x = 1 m and y = 0 m. Since the rem counters measure the total dose rate, the percent of neutron-scattered contribution to a total dose rate in Table 11 was calculated with the use of the uncollided dose rate shown in Table 10.

The Monte Carlo calculations of scattered doses in the +y and -x direction and toward the corners of the cell were not significantly different from those reported in the +x and -y direction at the same distance from the source position.

Table 10. Monte Carlo results

Detector position (metres)		$\left(\frac{\text{Dose-equivalent rate, mrem/hr}}{\text{source n/sec}}\right)$		% scattered contribution
x	y	Uncollided	Total	
1	0	$9.4587 \pm 0.0028 \times 10^{-7}$	$1.0162 \pm 0.0076 \times 10^{-6}$	6.92
2	0	$2.3117 \pm 0.0129 \times 10^{-7}$	$2.8268 \pm 0.0108 \times 10^{-7}$	18.2
3	0	$1.0278 \pm 0.0097 \times 10^{-7}$	$1.5840 \pm 0.0257 \times 10^{-7}$	35.1
4	0	$5.7336 \pm 0.0073 \times 10^{-8}$	$9.9634 \pm 0.0194 \times 10^{-8}$	42.5
5	0	$3.6346 \pm 0.0037 \times 10^{-8}$	$7.9533 \pm 0.0221 \times 10^{-8}$	54.3
0	-1	$9.5579 \pm 0.0118 \times 10^{-7}$	$1.0119 \pm 0.0118 \times 10^{-6}$	5.54
0	-2	$2.3437 \pm 0.0141 \times 10^{-7}$	$2.8317 \pm 0.0162 \times 10^{-7}$	17.2
0	-3	$1.0120 \pm 0.0107 \times 10^{-7}$	$1.5934 \pm 0.0243 \times 10^{-7}$	36.5

Table 11. Experimentally measured results

Detector position (metres)		$\left(\frac{\text{Dose-equivalent rate, mrem/hr}}{\text{source n/sec}}\right)$		Scattered contribution (%)	
x	y	Anderson-Braun	22.86-cm sphere	Anderson-Braun	22.86-cm sphere
1	0	1.02×10^{-6}	1.02×10^{-6}	6.92	6.92
2	0	3.26×10^{-7}	3.42×10^{-7}	29.1	32.4
3	0	1.77×10^{-7}	1.95×10^{-7}	42.0	47.3
4	0	1.21×10^{-7}	1.38×10^{-7}	52.6	58.5
5	0	9.48×10^{-8}	1.11×10^{-7}	61.7	67.3
0	-1	1.01×10^{-6}	1.02×10^{-6}	5.4	6.3
0	-2	3.29×10^{-7}	3.15×10^{-7}	28.8	25.6
0	-3	1.84×10^{-7}	1.80×10^{-7}	45.0	43.8

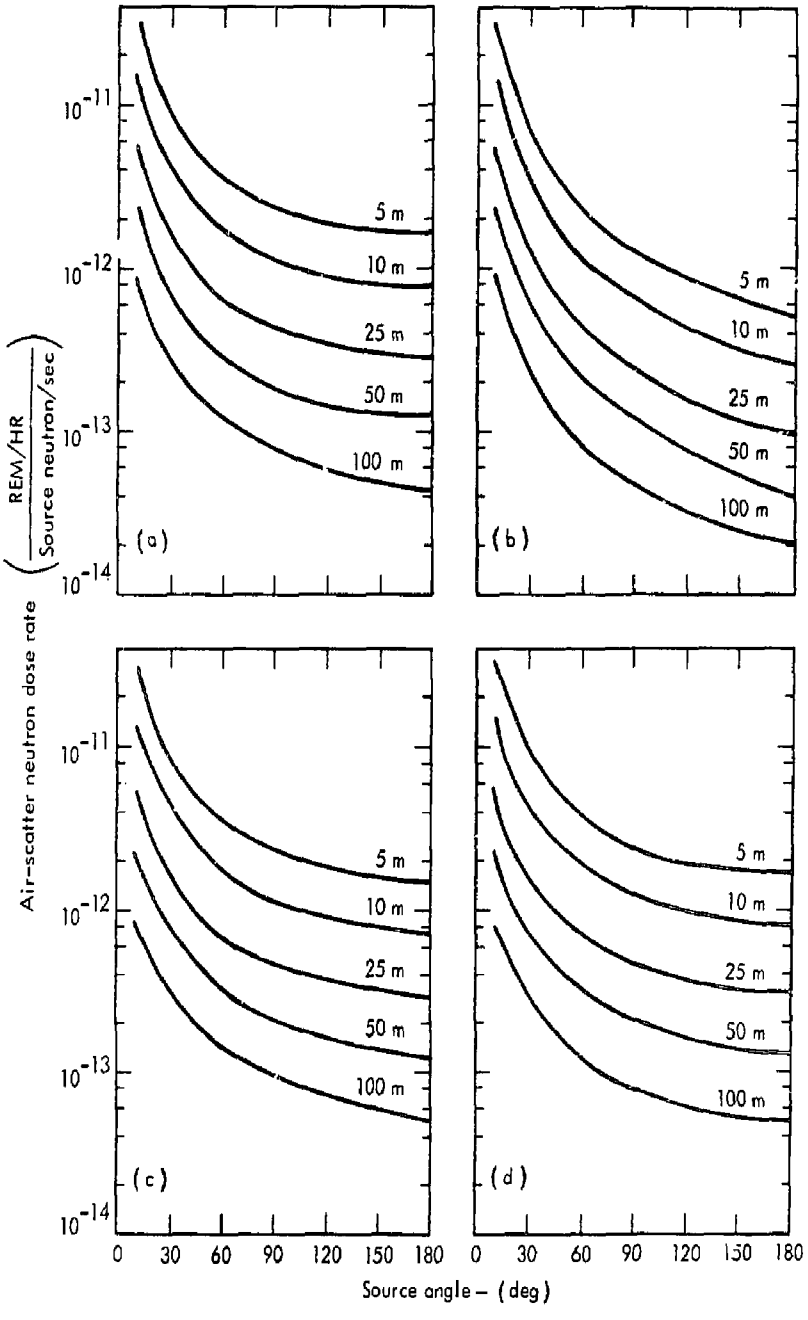

Fig. 32. Air-scattered fast neutron dose rates: (a) Pu Be; (b) 14 MeV; (c) 2.54 MeV; and (d) ^{252}Cf.

Air-Scattered Fast-Neutron Dose Rate

The air-scattered fast-neutron dose rate curves published in the Reactor Handbook[29] are frequently referred to by the Health Physics staff for the estimation of skyshine and related problems. These curves are based on calculations performed by Wells[30] in the late 1950's. Since that time, some changes have been made in scatter cross sections generally used. Wells also assumed a quality factor (Q.F.) of 10 for the flux- to biological-dose conversion. Recent calculations with the MORSE-L code[28] have differed from estimates made based on Blizard[29] by about a factor of two. Using MORSE-L, we have recalculated the air-scattered fast-neutron dose rate curves for those neutron sources most commonly encountered. For figures which follow (Fig. 32a-d), the source neutrons were directed along the "source angle." The resulting "air-scatter neutron dose rate" was calculated in Rem·hr^{-1}/source n·sec^{-1} at various distances from the source origin. The Q.F.'s used for the flux- to biological-dose conversion were interpolated from ICRP 21 "Data for Protection against Ionizing Radiation from External Sources," for the 30-group neutron structure reported by Wilcox.[31]

Twenty batches of 250 particles each were followed for each point at small angles. The batch size was increased to 500 particles for the larger scatter angles. The curves are drawn in on a visual best fit to the data.

Neutron Spectrum at the LPTR Fast Neutron Irradiation Facility

The Fast Neutron Irradiation Facility (FNIF) at the Livermore Pool-Type Reactor (LPTR) provides a high flux source of unmoderated fission spectrum neutrons for experiments such as materials damage studies. The FNIF, located in the east thermal column, involves the exposure of thermal neutrons to a pair of uranium-aluminum-alloy fission plates (Fig. 33). A boral shutter can be used to start and stop the FNIF exposures.

The neutron spectrum had been measured at the FNIF in 1968.[32] but changes in reactor configuration and lack of data below 0.01 MeV have contributed to the need for a new measurement. As with the previous one, the measurement was done with activation foils. The foils used (Table 12) include gold, iron, and indium which were not used before. We did not include magnesium and iodine this time because the ^{24}Mg(n,p)^{24}Na and ^{127}I(n,2n)^{126}I reactions are used as high-energy detectors, and were not really necessary for these measurements.

Measurements were made at 2.5 and 25 cm from the surface of the FNIF plate (Fig. 33). Six separate irradiations were made (Table 13) to include the use of all the foils. The measurements were made at reactor power levels between 3 kW and 3 MW, depending on the sensitivity of the foils used.

Results are normalized to 3 MeV. Cadmium, boron wafers and the boron spheres were used to impress a "threshold" structure on the ^{197}Au(n,γ)^{198}Au and ^{239}Pu(n, fission) response functions for low-energy spectrometry. We prefer this approach to the use of resonance detectors for measurement of neutrons from 10^{-6} to 10^{-2} MeV.

The activation foils, with the exception of sulfur pellets, are counted with a 7.6- × 7.6-cm NaI crystal, and the general method has been described

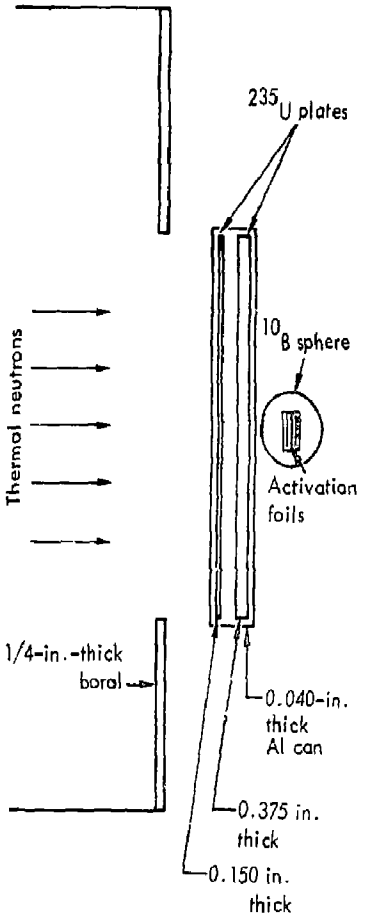

Fig. 33. LPTR Fast Neutron Irradiation Facility (FNIF).

Table 12. Activation foil summary

Foil	Reaction	Shield	Energy range (MeV)	Weighted cross sections (barns)
Au	$^{197}Au(n,\gamma)^{198}Au$	None	Thermal	67
Au	$^{197}Au(n,\gamma)^{198}Au$	Cd-0.051 cm	$\geq 0.4 \cdot 10^{-6}$	Used for LOUHI calculations only
Au	$^{197}Au(n,\gamma)^{198}Au$	^{10}B-0.23 g·cm^{-2}	$\geq 10^{-5}$	Used for LOUHI calculations only
Pu	$^{239}Pu(n,fission)$	^{10}B-1.65 g·cm^{-2}	≥ 0.01	1.70
Np	$^{237}Np(n,fission)$	$^{10}B^a$	≥ 0.60	1.65
In	$^{115}In(n,n')^{115}In$	$^{10}B^a$	≥ 1.0	0.24
U	$^{238}U(n,fission)$	$^{10}B^a$	≥ 1.5	0.55
Fe	$^{54}Fe(n,p)^{54}Mn$	$^{10}B^a$	≥ 2.5	0.30
S	$^{32}S(n,p)^{32}P$	$^{10}B^a$	≥ 3.0	0.30
Al	$^{27}Al(n,\alpha)^{24}Na$	$^{10}B^a$	≥ 7.5	0.07
Zr	$^{90}Zr(n,2n)^{89}Zr$	$^{10}B^a$	≥ 14.0	2.0

[a] ^{10}B used for threshold detectors to suppress possible contaminants from thermal reactions.

Table 13. FNIF run summary

Run	Reactor power (MW)	Irradiation time (sec)	Foils used	Distance to plate (cm)
1	0.003	600	Au,S	2.5
2	0.003	1800	Au,S	25
3	0.03	600	Pu,Np,U,In,S	2.5
4	0.03	600	Pu,Np,U,In,S	25
5	3.0	600	Al,Zr,Fe,In,S	2.5
6	3.0	1800	Al,Zr,Fe,In,S	25

Table 14. Summary of FNIF flux measurements (n·cm^{-2}·sec^{-1}@ 3 MW × 10^{10})

Energy (MeV)	2.5 cm		25 cm	
	New	1968 values	New	1968 values
$\leq 0.4 \cdot 10^{-6}$	0.82	–	0.28	–
≥ 0.01	3.58	2.64	0.64	0.47
≥ 0.6	2.64	2.19	0.37	0.36
≥ 1.0	2.21	–	0.274	–
≥ 1.5	1.54	1.36	0.185	0.203
≥ 2.5	0.84	–	0.088	–
≥ 3.0	0.64	0.60	0.067	–
≥ 7.5	0.026	0.022	0.0025	0.0025
≥ 14.0	0.00012	0.00011	0.000011	–

before.[32,33] The sulfur pellets are counted with a gas flow proportional counter, while the fission foils are evaluated by track registration which has also been described before.[32]

Preliminary flux estimates were made using the familiar activation equation:*

$$\phi = \frac{Ce^{\lambda t}}{\sigma \cdot E \cdot N(1 - e^{-\lambda T})}$$

where ϕ = neutron flux,

C = measured activity in net counts per second at time t,

λ = decay constant of the induced activity,

t = time elapsed from the end of the irradiation to the midpoint of the count,

σ = reaction cross section,

E = overall counting efficiency,

N = number of atoms of the parent isotope present,

T = length of the irradiation time.

The results of these estimates are shown in Table 14 with previous values for comparison.

A more aesthetic, if not more informative spectrum estimate was made with the LOUHI computer unfolding code.[34] LOUHI, which has been described in a number of recent progress reports,[33,35,36] evaluates equations of the form

$$A_j = C_j \sum_{n=1}^{k} \sigma_{jn} \phi_n \Delta E_n$$

where A_j = response of the jth detector,

C_j = a normalizing factor,

σ_{jn} = response of the jth detector in the nth energy band,

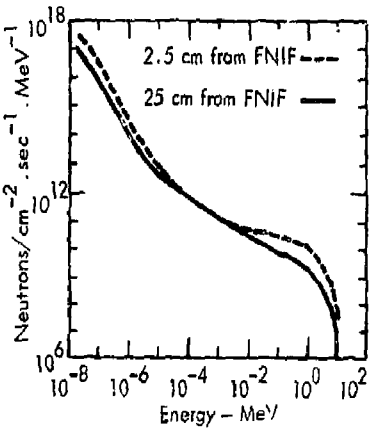

Fig. 34. Differential neutron spectra from FNIF at 3 MW.

ϕ_n = flux or fluence in the nth energy band,

and ΔE_n = width of the nth energy band.

We have gained confidence in LOUHI from previous measurements by comparison of computed spectra with hand-calculated values and, in some cases, computer predictions of the spectra. The LOUHI calculated values for the FNIF also seem to be in good agreement with hand-calculated values. Figure 34 shows the computer-produced spectrum. The differential and integral values are presented in Table 15.

The overall results show a slight increase in flux levels over the 1968 values, with the most pronounced increase occurring below 0.5 MeV. The LOUHI integral values are lower than the hand-calculated values by 10% to 15% up to 7.5 MeV. The two high-energy bins which correspond roughly to the aluminum and zirconium results are low by a factor of two or more. We suspect the low values may be an artifact of the calculation associated with the high-energy bin, and should be used with caution.

*The irradiations were short compared with the half-lives of the induced isotopes, so $(1 - e^{\lambda T})$ is approximated by λT and t is taken from the midpoint of the irradiation.

Table 15. LOUHI calculated FNIF fluxes at 3 MW

Lower energy bond (MeV)	Differential flux in energy bond ($n \cdot cm^{-2} \cdot sec^{-1} \cdot MeV^{-1}$)		Integral flux (> E) ($n \cdot cm^{-2} \cdot sec^{-1} \times 10^{10}$)	
	2.5 cm	25 cm	2.5 cm	25 cm
2.5×10^{-8}	$2.15 \cdot 10^{17}$	$7.56 \cdot 10^{16}$	4.37	0.990
4.2×10^{-8}	$7.22 \cdot 10^{16}$	$2.49 \cdot 10^{16}$	4.01	0.861
7.0×10^{-8}	$2.44 \cdot 10^{16}$	$8.25 \cdot 10^{15}$	3.80	0.792
1.2×10^{-7}	$8.38 \cdot 10^{15}$	$2.79 \cdot 10^{15}$	3.68	0.750
1.9×10^{-7}	$2.95 \cdot 10^{15}$	$9.73 \cdot 10^{14}$	3.63	0.731
3.2×10^{-7}	$1.07 \cdot 10^{15}$	$3.66 \cdot 10^{14}$	3.59	0.718
5.4×10^{-7}	$4.07 \cdot 10^{14}$	$1.38 \cdot 10^{14}$	3.56	0.711
9.0×10^{-7}	$1.63 \cdot 10^{14}$	$5.74 \cdot 10^{13}$	3.55	0.706
1.5×10^{-6}	$6.91 \cdot 10^{13}$	$2.58 \cdot 10^{13}$	3.54	0.702
2.5×10^{-6}	$3.12 \cdot 10^{13}$	$1.26 \cdot 10^{13}$	3.53	0.699
4.2×10^{-6}	$1.50 \cdot 10^{13}$	$6.69 \cdot 10^{12}$	3.52	0.697
7.0×10^{-6}	$7.74 \cdot 10^{12}$	$3.87 \cdot 10^{12}$	3.52	0.695
1.2×10^{-5}	$4.22 \cdot 10^{12}$	$2.39 \cdot 10^{12}$	3.52	0.693
2.0×10^{-5}	$2.43 \cdot 10^{12}$	$1.57 \cdot 10^{12}$	3.52	0.692
3.2×10^{-5}	$1.47 \cdot 10^{12}$	$1.07 \cdot 10^{12}$	3.51	0.690
5.4×10^{-5}	$9.27 \cdot 10^{11}$	$7.54 \cdot 10^{11}$	3.51	0.687
9.1×10^{-5}	$6.07 \cdot 10^{11}$	$5.39 \cdot 10^{11}$	3.51	0.684
1.5×10^{-4}	$4.10 \cdot 10^{11}$	$3.83 \cdot 10^{11}$	3.50	0.681
2.5×10^{-4}	$2.84 \cdot 10^{11}$	$2.78 \cdot 10^{11}$	3.50	0.677
4.2×10^{-4}	$2.02 \cdot 10^{11}$	$1.97 \cdot 10^{11}$	3.49	0.673
7.0×10^{-4}	$1.47 \cdot 10^{11}$	$1.37 \cdot 10^{11}$	3.49	0.667
1.2×10^{-3}	$1.09 \cdot 10^{11}$	$9.48 \cdot 10^{10}$	3.48	0.660
2.0×10^{-3}	$8.24 \cdot 10^{10}$	$6.49 \cdot 10^{10}$	3.47	0.652
3.2×10^{-3}	$6.36 \cdot 10^{10}$	$4.44 \cdot 10^{10}$	3.46	0.645
5.4×10^{-3}	$5.02 \cdot 10^{10}$	$3.06 \cdot 10^{10}$	3.45	0.636
9.2×10^{-3}	$4.05 \cdot 10^{10}$	$2.14 \cdot 10^{10}$	3.43	0.624
1.5×10^{-2}	$3.34 \cdot 10^{10}$	$1.53 \cdot 10^{10}$	3.41	0.611
2.5×10^{-2}	$2.83 \cdot 10^{10}$	$1.12 \cdot 10^{10}$	3.37	0.596
4.2×10^{-2}	$2.45 \cdot 10^{10}$	$8.54 \cdot 10^{9}$	3.32	0.577
7.1×10^{-2}	$2.17 \cdot 10^{10}$	$6.68 \cdot 10^{9}$	3.25	0.552
1.2×10^{-1}	$1.94 \cdot 10^{10}$	$5.34 \cdot 10^{9}$	3.14	0.519
2.0×10^{-1}	$1.75 \cdot 10^{10}$	$4.30 \cdot 10^{9}$	2.99	0.476
3.3×10^{-1}	$1.54 \cdot 10^{10}$	$3.37 \cdot 10^{9}$	2.76	0.421
5.5×10^{-1}	$1.28 \cdot 10^{10}$	$2.46 \cdot 10^{9}$	2.43	0.347
9.2×10^{-1}	$9.39 \cdot 10^{9}$	$1.54 \cdot 10^{9}$	1.95	0.255
1.5×10^{0}	$5.74 \cdot 10^{9}$	$7.72 \cdot 10^{8}$	1.41	0.166
2.6×10^{0}	$3.44 \cdot 10^{9}$	$3.73 \cdot 10^{8}$	0.774	0.0812
4.2×10^{0}	$7.11 \cdot 10^{8}$	$6.89 \cdot 10^{7}$	0.225	0.0219
7.2×10^{0}	$2.24 \cdot 10^{7}$	$2.11 \cdot 10^{6}$	0.0108	0.00102
1.2×10^{1} to 1.8×10^{1}	$1.62 \cdot 10^{5}$	$1.47 \cdot 10^{4}$	0.00013	0.000012

Monitoring Ground Water for Pesticide Residues

Pesticide use on the LLL grounds is highly diverse, and over the past several years has included more the 35 different materials. These consist principally of herbicides and fungicides, but also include some insecticides, notably chlordane and malathion. Most of these materials do not show a regular pattern of heavy use, and are not expected to accumulate in the soil and ground water. In addition, the persistence of most herbicides is markedly lower than that of chlorinated hydrocarbon insecticides such as dieldrin or DDT.[37]

Several routes exist by which pesticides, once applied, can leave the site: Entrainment in surface runoff water, evaporation, and a number of degradation pathways including microbial/enzymatic, solar irradiation photolysis, and hydrolysis reactions. Of these, the first was of primary interest to us, and a study of the effect of pesticides on the local ground water was begun in 1973.

Because of the variety of chemicals to be determined, a versatile analytical system consisting of a Finnigan 3000D gas chromatograph/mass spectrometer was used. Surface water samples were taken at the northwest corner of the site where the storm drain runoff leaves the LLL grounds. Sampling included the first and second surface runoffs of the season, which were expected to contain the highest contaminant levels. A combined 10-litre sample was multiply batch-extracted with ether, which in turn was dried and reduced in volume in a rotary evaporator at reduced pressure. Final volume was 1 ml, providing a concentration factor of 10^4.

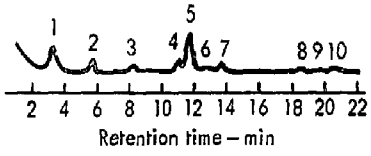

Fig. 35. Total ion current chromatograph of drainage ditch extract. Peaks 1,5: phthalate esters. Peaks 2,3,4,6,7: hydrocarbons. Peaks 8,9,10: polychlorinated biphenyls.

Most of the compounds of interest were directly chromatographable without further treatment. Samples 1 μl in size were injected onto a 3% OV-1 (methylsilicone) column which was temperature-programmed from 50°C to 190°C. A total ion current chromatogram is shown in Fig. 35.

Results. No residues of pesticides used at LLL were detected in the concentrated extract. Chromatographically separated materials in concentrations sufficient for mass spectrometric identification were either hydrocarbons or phthalate esters. Materials leached from roadways and roofs are the most probable sources of the hydrocarbons, while the phthalates were at least in part introduced from plastic materials used in handling the sample. Steps have been taken to reduce this source of contamination in future analyses.

Limited mass searches were made for molecular fragments diagnostic of polychlorinated biphenyls. By focusing on a narrow characteristic range of m/e, detection efficiency is greatly increased. The molecular ions of tetra- and hexa-chlorinated biphenyls have m/e ratios of 290 and 358 amu, respectively. Several chromatographic fractions at high temperature showed evidence of both these moieties, and thus of polychlorinated biphenyls, at the 10-100 parts per trillion level in the original sample.

The origin of these materials is problematical, since they are so widely used and dispersed in the environment. It would seem, however, that the levels found by us at LLL approximate normal background, based on levels reported for seawater.[38]

Total outflow of water, and thus of entrained materials, from the Laboratory grounds unfortunately cannot be measured. The future installation of a gaging station would permit such an estimate and the assignment of a probable upper limit to outflow of entrained contaminants. Monitoring of the ground water has been resumed on a quarterly basis during the 1975 calendar year.

Calibration of Proportional Counters for Neutron Spectrometer

A neutron spectrometer system has been developed at LLL for use as a health physics instrument. It has a variety of types of detector, including several proportional counters. To reduce the data obtained with this system as well as to optimize performance, the characteristics of each detector have been determined with respect to:

- Neutron detection efficiency.
- Pulse height resolution as a function of anode voltage.
- Gas multiplication factor as a function of anode voltage.

In addition, for measurements in the field it has been necessary to develop a method of system energy calibration which is independent of available neutron sources. This report concerns the resolution and gas multiplication characteristics of the proportional counters used in the spectrometer system.

Experiments. Several proportional counters were exposed to highly thermalized neutrons provided by moderated ^{252}Cf and PuBe sources. The (n,p) reactions with thermal neutrons in nitrogen gas (a 5% constituent of hydrogen proportional counters) or in ^{3}He produce ionizing charged particles which deposit a fixed amount of energy in the detector. The effective energy deposited[39,40] is:

$^{14}N\ (n,p)^{14}C$	615 keV
$^{3}He\ (n,p)^{3}H$	770 keV

A peak is produced in the pulse height spectra obtained under these conditions. Its location is dependent upon electronic gain and detector gas multiplication. The width is indicative of the system energy resolution.

Each detector was calibrated as follows: Pulse-height spectra were obtained at different anode voltages using a charge-sensitive preamplifier and conventional spectroscopy electronics. The FWHM of the (n,p) reaction peak was measured, the centroid was located, and the zero energy intercept was determined using a linear pulser. To determine the charge collected following an (n,p) reaction, a "tail pulser" was adjusted to deposit an equal charge at the preamplifier input through a small calibrated coupling capacitance. The shape of the pulser output was adjusted to resemble the detector charge output, i.e., $\tau_{rise} \sim 5\ \mu s$ and $\tau_{fall} \sim 1000\ \mu s$. Calculation of the charge deposited was carried out according to Eq. (1) below:

$$Q = CV \tag{1}$$

where C = coupling capacitance,
V = peak pulser voltage.

At each anode voltage, the gas multiplication factor was calculated according to Eq. (2) below:

$$G = \frac{\text{charge collected}}{\text{initial charge produced}} = \frac{Q}{\frac{E_0}{W_0}e} \tag{2}$$

where E_0 = effective energy deposition,
W_0 = mean ionization energy of the gas,[41]
e = electronic charge.

Results. Physical parameters describing each detector are given in Table 16. Results of the resolution measurements are shown in Fig. 36. At low anode voltage, resolution is limited by electronics noise since the gas multiplication is low and output pulses are small. Resolution at large anode voltages is presumably limited by non-uniformities in gas multiplication and charge collection. The data shown may be used to establish a proper anode voltage for optimum resolution.

Results of the gas multiplication measurements are shown in Fig. 37. An attempt has been made to fit the gas multiplication data for each detector to the well known analytical relation of Diethorn:[42]

$$\log G = V\,[a \log V + b] \tag{3}$$

where a,b are parameters,

V = anode voltage,
G = gas multiplication factor.

Data obtained for the hydrogen proportional counters fit this relation well, as does the ^{3}He data at large gas multiplication. Values for the parameters a and b based on least-squares fits to the data are included in Table 12. At low multiplication, the ^{3}He proportional counters deviate from Eq. (3). Hopstone[43] has proposed an improved relation [Eq. (4)] for ^{3}He.

Table 16. Proportional counter characteristics

Length of sensitive volume, L (cm)	Cathode diameter, D (cm)	Anode diameter, d (mm)	Gas fill	Diethorne[39] a	Parameters b
25.4	3.81	0.025	3 atm H_2 0.13 atm N_2 0.13 atm CH_4	2.10×10^{-3}	-0.015
45.7	5.08	0.025	20 atm H_2 1 atm N_2	1.4×10^{-5}	-8.1×10^{-5}
45.7	5.08	0.051	4 atm ^3He 4 atm A_r	2.20×10^{-3}	-0.016
15.2	2.5	–	4 atm ^3He	4.32×10^{-3}	-0.027
45.7	5.08	0.025	4 atm ^3He Δ atm Kr	2.43×10^{-3}	-0.017

$$V = a\left[P\,d\log\frac{D}{d}\right]^{0.35}[\log G]^{0.45} + b\left[P\,d\log\frac{D}{d}\right] \qquad (4)$$

where a, b are parameters,

P = total gas pressure,
D,d = cathode and anode diameters, respectively respectively,
V = anode voltage.

Determination of parameters a,b for our ^3He proportional counters is in progress.

Conclusion. Laboratory energy calibration of hydrogen or ^3He proportional counters is normally accomplished by locating a peak in the pulse-height

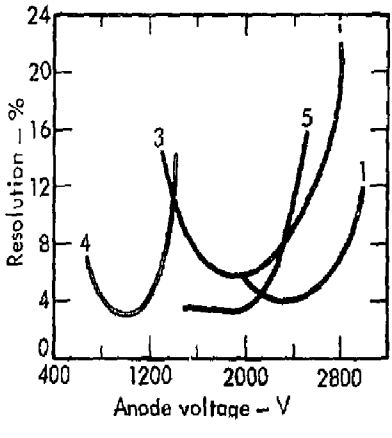

Fig. 36. Proportional counter resolution versus anode voltage.

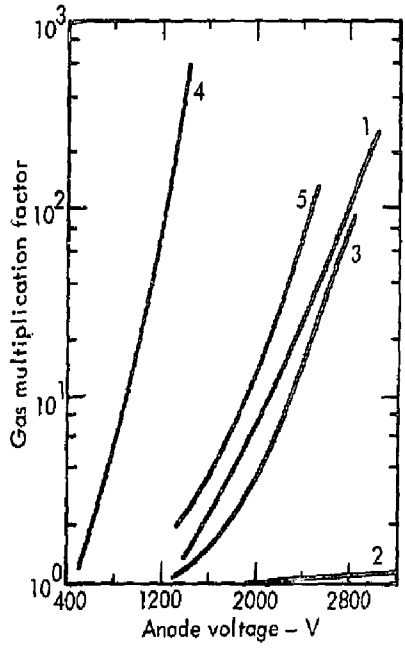

Fig. 37. Proportional counter gas multiplication factor.

spectrum due to the (n,p) reaction with thermal neutrons. However, when these detectors are used for field measurements, a suitable source of thermal neutrons is often not available. Alternatively, the gas multiplication characteristics shown in Fig. 37 may be used to establish a relation between energy deposited in the detector and the amplitude of detector output. Energy calibration is then accomplished by using a pulser to deposit a known charge at the preamp input and adjusting the electronics gain for a desired pulse height at the analyzer. Figure 37 is then used to relate the known charge input to an equivalent energy deposition in the detector. An energy calibration is then obtained without a source of thermal neutrons.

Decontamination of Gloved Boxes by Acid Wash

Waste material contaminated with more than 10 nCi of transuranium isotopes per gram of waste has to be packaged to remain intact and transportable after 20 years of storage at an ERDA-controlled site. ERDA also wants the volume of waste that requires retrievable storage to be reduced.

Gloved boxes used for work with transuranium isotopes invariably become more highly contaminated than 10 nCi/g. Decontamination is the only way to avoid the expense of packaging such gloved boxes for long-term storage. The usual method of decontaminating gloved boxes is to wipe all surfaces with swabs of absorbent paper wetted with a solvent or with a detergent solution. Wiping is repeated until the concentration of contaminant has been reduced to the desired level. This is a tedious and time-consuming procedure. Frequently, it is the only acceptable method when the equipment inside is costly and must be retained. However, discarded gloved boxes need not be treated so gently. We have devised a method to decontaminate such gloved boxes quickly and with a minimum of effort.

Rapid decontamination is achieved with an acid spray treatment. The spray solution is 30% nitric acid with 1% of hydrofluoric acid added. A 6-mm (1/4-in.) pliable plastic tube is inserted through a convenient opening or through a hole made in a glove or in a window. For a gloved box of normal size, about 1 litre of acid solution is pumped into the box with a small rubber-vaned pump. The operator constructs the end of the tubing to produce a fine jet and directs the acid to all internal surfaces of the box. When all surfaces have been wetted, the box is allowed to stand about an hour to give the acid time to dissolve the transuranium isotope lodged in the surface pores of the box materials.

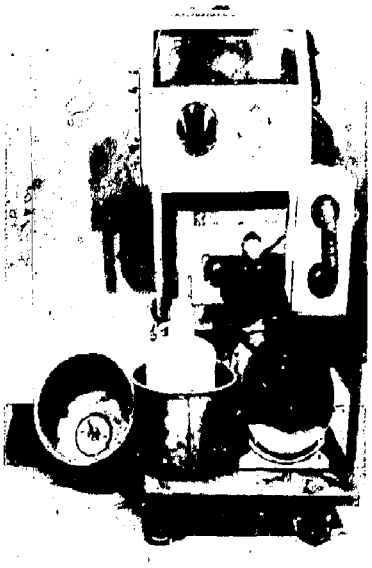

Fig. 38. Acid decontamination system for gloved boxes.

Much of the acid drains to the floor of the box. This is not a loss since the floor is usually more highly contaminated than any other part of the box. The acid

Table 17. Summary of decontamination of gloved boxes by an acid wash method

	Contamination			
	^{239}Pu (9 boxes)		^{233}U (3 boxes)	
	Average	Range	Average	Range
Initial contamination determined by swipe samples (dpm/cm^2)	4×10^5	10^4-10^6	8×10^5	10^5-10^6
Direct reading with alpha probe after acid wash (dpm, cm^2)	7×10^3	10^2-10^4	3×10^3	50-10^4
Total activity removed as determined with a drum counter				
Liquid waste (dpm)	10^{11}	8×10^{10}-2×10^{11}	6×10^{10}	10^{10}-8×10^{10}
Dry waste, including box gloves (dpm)	2×10^{10}	10^9-8×10^{10}	2×10^{10}	2×10^9-4×10^{10}

solution is removed through another plastic tube to a 20-litre (5-gal) plastic carboy by suction. The system is shown open in Fig. 38. The carboy is enclosed in a metal container with the end of the suction tubing well down in the neck. A vacuum pump evacuates the metal container to provide suction for the tubing that removes the acid solution from the box. An in-line filter protects the vacuum pump from contamination, and a small HEPA filter on the exhaust of the pump provides backup protection against the release of contaminant into the room. When the acid solution has been removed, the interior is sprayed with water to wash away the residual acid. The rinse water is removed to the carboy by the suction system. The interior is rinsed again and the water is removed by suction. The visible water remaining is removed with absorbent paper wipes. When the interior has air-dried, an alpha survey meter probe is inserted to make a direct check of the concentration of the contamination that remains. If the level is not below 10 nCi/cm^2, the acid wash is repeated. When the level is low enough, the box gloves are removed since they retain considerable fixed contaminant.

Since May 1974, twelve gloved boxes have been contaminated by this method. In only one instance was it necessary to repeat the acid wash. After decontamination by this method, the gloved boxes were disposed of in the less costly packaging required for burial of radioactive waste at a commercial disposal site.

A summary of the radioactivity levels during decontamination of the gloved boxes appears in Table 17. The values have been rounded off in view of the uncertainties inherent in trying to obtain representative samples. However, in each case the weight of the gloved box was well over 1 g/cm^2, so all the boxes were decontaminated well below the level requiring retrievable storage.

Decontamination of a gloved box by the acid wash method takes about one man-day of effort. Packaging a gloved box for retrievable storage costs the equivalent of nearly two man-months. Packaging the gloved box to also meet the transportation regulations costs well over a man-year. Decontamination of a gloved box reduces the volume that has to be placed in retrievable storage by a factor of 100.

Publications

G. O. Nelson and R. D. Taylor, *Chlorine and Hydrogen Chloride Testing System Revised Operating Manual*, Lawrence Livermore Laboratory, Rept. M-060 (1975).

The Chlorine and Hydrogen Chloride Cartridge Testing System measures the effective cartridge and canister service life under the conditions set forth in Title 30 CFR Part 11. A cartridge is subjected to test concentrations of 0.05, 0.5, or 2.0% at 32 or 64 litres/min and 50% relative humidity. An analyzer is placed downstream of the cartridge, and the effluent concentration is monitored as a function of time. Upstream and downstream temperatures are measured continuously throughout the test.

T. R. Crites, *An Experimental Study of the Energy Dependence of an Albedo-Type Neutron Dosimeter*, Lawrence Livermore Laboratory, Rept. UCRL-77028 (1975).

The response of a simple albedo-type personnel neutron badge was experimentally determined using various neutron spectra. The energy dependence of this type badge is discussed relative to dose-equivalent determinations. Computer calculations were performed to substantiate trends found experimentally.

T. M. Distler and Y. M. Kwok, *Toxic Vapor Hazard of Heated Mock High Explosive*, Lawrence Livermore Laboratory, Rept. UCID-16769 (1975).

Three types of mock high explosives, 90503, LM-04, and RM-04-BF, were pyrolyzed in a temperature range between 200° and 700°C, and the gaseous products were then analyzed. Isocyanic acid, hydrogen cyanide, and cyanogen were found in the product gases.

J. R. Gaskill, M. W. Magee and R. G. Purington, *Phenomena Observed with the Use of Halon 1301 on Burning Explosives*, Lawrence Livermore Laboratory, Rept. UCRL-76941 (1975) (submitted to Fire Technology).

To answer the question as to whether Halon 1301 would be effective in extinguishing burning explosives, 0.5-kg samples of three different explosive formulations were individually ignited in a large cubical box; in each case after the material was burning, the box was flooded with 70% (vol) of Halon. In two cases out of three, the fire was not extinguished. Furthermore, large quantities of bromine gas were generated. This gas production can cause a hazard to unprotected firefighters.

Walter L. Eneidi, Robert D. Taylor, *an Air-Purifying Powered Respirator Pack*, Lawrence Livermore Laboratory Rept. UCRL-75183 (1975)(submitted to the American Industrial Hygiene Assn. Journal).

Design and construction of a moderate-weight, battery-powered respirator pack is described. Two variations have been fabricated. One weighs 9 lb and is able to maintain positive pressure within a full face mask for 4 1/2 hr, while the larger unit which weighs 15 lb is usable for approximately 10 hr.

R. V. Griffith, D. R. Slaughter and T. R. Crites, *LLL Special Projects Division Research in Neutron Measurements Techniques*, Lawrence Livermore Laboratory, Rept. UCRL-76944 (1975) (submitted to Fifth ERDA Workshop on Personnel Neutron Dosimetry, Washington D. C., May 6 and 7, 1975).

Recent work in neutron dosimetry and spectrometry development is summarized. Brief discussions are presented on multisphere systems, high-resolution spectrometers, an albedo dosimeter and track etch detectors for personnel dosimetry.

Dale E. Hankins, *Studies of Neutron Dosimetry at the Lawrence Livermore Laboratory*, Lawrence Livermore Rept. UCRL-76808 (1975) (presented at the Fifth Workshop on Personnel Neutron Dosimetry, Gaithersburg, Md., May 6-7, 1975).

Several aspects of neutron dosimetry were studied and are included in this report. These are: (1) A procedure for the evaluation of neutron exposures by using the results obtained from the LLL personnel TLD badges. Since the TLD badge responds primarily to thermal neutrons, a method of relating the readings from the badge to neutron exposures had to be established. (2) A summary was given of the results obtained from studies at reactors, plutonium facilities, storage areas, accelerators and radiochemistry buildings to determine the calibration factors that would be applicable for each facility. The differences in these calibration factors are used to evaluate the usefulness of albedo neutron dosimeters at those facilities. (3) Additional information on the directional response and the energy dependence of four neutron rem meters was presented.

Yen Mee Kwok, *Evaluation of the Spectrophotometric Determination of Traces of Selenium with 2,3-Diaminonaphthalene*, Rept. UCRL-77017 (1975)(submitted to Analytical Chemistry).

The tentative method of analysis for selenium content of atmospheric particulate matter is a photometric procedure which requires separation of foreign elements from the reaction solution. This study was done to evaluate the method which was ultimately modified for the analysis of selenium in sewer water.

D. S. Myers, *The Biological Hazard and Measurement of Plutonium*, Lawrence Livermore Laboratory, Rept. UCRL-76571 (1975) (presented at the Radiological Defense Officer's Conference, South Lake Tahoe, Oct. 23-25, 1974).

Ever since its production in 1941 by Glen Seaborg and his co-workers, the element plutonium has received a great deal of attention. As the amount of plutonium in the global inventory has increased and its applications have become more widespread, research involving and controversy surrounding this element have been further intensified.

This paper briefly summarizes (1) the basic characteristics of plutonium including its uses, its physical and chemical properties, and the types and amounts of radiation it emits; (2) the biological effects associated with exposure to plutonium; and (3) the techniques for measuring plutonium. The emphasis is on the measurement of plutonium with portable instruments in the field.

Byron N. Odell, *Supporting Documents for LLL Safety Analysis Reports Livermore Site*, Lawrence Livermore Laboratory, Rept. UCRL-51801 (1975).

The following appendices are common to the LLL Safety Analysis Reports Livermore Site, and are included here as supporting documents to those reports.

A Description, Population Distribution, and Land Use
B A Geological and Seismological Investigation of the Lawrence Livermore Laboratory Site
C Meteorology
D Tornado Criteria for the LLL Site (To be supplied)
E Characteristics of California Tornados
F Surface Water Hydrology
G Ground Water Hydrology
H Lawrence Livermore Laboratory Quality Assurance Program
I Environmental Monitoring at the Lawrence Livermore Laboratory 1974 Annual Report.

R. G. Purington, *Friction-Loss Studies Using a 0.0127-m Fire Hose*, Lawrence Livermore Laboratory, Rept. UCRL-76511 (1975) (submitted to Fire Technology).

Friction loss studies using polyethylene oxide injected into a 0.0127-m fire hose show about a 45% reduction in friction loss.

W. J. Silver, C. L. Lindeken, J. W. Meadows, E. H. Willes and D. R. McIntyre, *Environmental Monitoring at the Lawrence Livermore Laboratory, 1974 Annual Report*, Lawrence Livermore Laboratory, Rept. UCRL-50027-74 (1975).

An environmental surveillance program is conducted at Lawrence Livermore Laboratory to ensure that the Laboratory's effluent control program is indeed restricting the release of effluents from the Livermore site and Site 300 to concentrations well below applicable standards. The program includes the collection and analysis of air, soil, water, sewer effluent, vegetation, and milk samples. Environmental background radiation is measured at numerous locations in the vicinity of the Laboratory by means of thermoluminescent detectors. The results of the analyses are provided in this report.

References

1. Dale E. Hankins, "The Energy Response of TLD Badges Located on Personnel," *Health Phys.* **28**, 80 (1975).
2. D. Newton, F. A. Fry, B. T. Taylor, M. C. Eagle, and R. C. Sharma, "Interlaboratory Comparison of Techniques for Measuring Lung Burdens of Low-Energy X-ray Emitters," *Twentieth Annual Health Physics Society Meeting, Buffalo, N. Y. July 1975*
3. *Radiological Health Handbook*, U. S. Department of Health, Education and Welfare (January 1970).
4. P. G. Kase, *Computerized Anatomical Model Man*, Air Force Weapons Laboratory, Kirtland AFB, N. M., Rept. AFWL TR-69-161 (1970).
5. A. C. Eycleshymer and D. M. Schoemaker, *A Cross-Section Anatomy* (Appleton-Century-Crofts, 1970).
6. A. J. Stacey, A. R. Bevan, and C. W. Dickens, "A New Phantom Material Employing Depolymerized Natural Rubber," *Brit. J. Radiology* **34**, 510 (1961).
7. D. E. A. Jones and H. C. Raines, *Brit. J. Radiology* **22**, 549 (1949).
8. *Hazards Control Progress Report No. 49*, Lawrence Livermore Laboratory, Rept. UCRL-50007-75-1 (1975), pp. 4-5.
9. G. O. Nelson and C. A. Harder, "Respirator Cartridge Efficiency Studies: V. Effect of Concentration," *Am. Ind. Hygiene Assn. J.* **35**, 391 (1974).
10. *Hazards Control Progress Report No. 48*, UCRL-50007-74-1 (1974), p. 11-15.
11. *Hazards Control Progress Report No. 44*, Rept. UCRL-50007-72-3 (1972), p. 15.
12. *Hazards Control Progress Report No. 46*, Rept. UCRL-50007-73-2 (1973), p. 11.
13. *Hazards Control Progress Report No. 47*, Rept. UCRL-50007-73-3 (1973), p. 14.
14. *Hazards Control Progress Report No. 48*, p. 20.
15. *Hazards Control Progress Report No. 49*, p. 13.
16. *Hazards Control Progress Report No. 50*, UCRL-50007-75-1 (1975).
17. D. R. Slaughter, D. W. Rueppel, "Calibration of Proportional Counters for Neutron Spectrometer," *Hazards Control Progress Report No. 50.*
18. *Hazards Control Progress Report No. 44*, p. 15.
19. *Hazards Control Progress Report No. 46*, p. 11.
20. *Hazards Control Progress Report No. 47*, p. 14.
21. *Hazards Control Progress Report No. 48*, p. 20.
22. *Hazards Control Progress Report No. 49*, p. 13.
23. V. V. Verbinski *et al. Nucl. Instr. Methods* **65**, 8 (1968).
24. E. F. Bennett and T. J. Yule, *Techniques and Analyses of Fast Reactor Neutron Spectroscopy with Proton Recoil Proportional Counters*, Argonne National Laboratory, Rept. ANL-7763 (1971).
25. J. R. Gaskill, "Smoke Development in Polymers during Pyrolysis or Combustion," *J. Fire and Flammability*, **1**, 183 (1970).
26. J. R. Gaskill and C. R. Veith, "Smoke Opacity from Certain Woods and Plastics," *Fire Technology*, **4**, 185-195, August 1968.
27. Hazards Control Progress Report No. 43, UCRL-50007-72-2 (1972).
28. T. P. Wilcox, *Morse-L, A Special Version of the Morse Program Designed to Solve Neutron, Gamma, and Coupled Neutron-Gamma Penetration Problems*, Mor-6, Lawrence Livermore Laboratory, Rept. UCID-16680 (1972).
29. E. P. Blizard, Ed., *Reactor Handbook* Vol. III, Part B, "Shielding" 1962.
30. M. B. Wells, *Monte Carlo Calculations of Fast Neutron Scattering in Air, Vol. I; Analysis*. Convair, Rept. NARF-60-8T (FZK-9-147), (May 13, 1960).
31. T. P. Wilcox, *MORSE Cross Section Tapes, MOR-13*, Lawrence Livermore Laboratory, Rept. UCID-16683 (1973).
32. *Hazards Control Progress Report No. 32*, UCRL-50007-68-3 (1968), p. 17.
33. *Hazards Control Progress Report No. 49*, p. 41.
34. J. T. Routti, "Mathematical Consideration of Determining Neutron Spectra from Activation Measurements," *Proc. Second Intern. Symp. Accelerator Dosimetry and Experience*, Stanford University, November 5-7, 1969, Paper CONF-691101.

35. *Hazards Control Progress Report No. 48*, p. 8.
36. *Hazards Control Progress Report No. 49*, p. 34.
37. C. A. Edwards, *Persistent Pesticides in the Environment*, 2nd ed. (CRC Press, Chemical Rubber Co., Cleveland, Ohio 2973), p. 107.
38. *Finnigan Spectra 2 No. 3*, Finnigan Corp., Sunnyvale, Calif. (1972), p. 2.
39. E. F. Bennett and T. J. Yule, *Techniques and Analyses of Fast Reactor Neutron Spectroscopy With Proton-Recoil Proportional Counters*, Argonne National Laboratory, Rept. ANL-7763 (1971).
40. R. Batchelor and G. C. Morrison, "Helium-3 Neutron Spectrometers," *Fast Neutron Physics Part I*, J. B. Marion and J. L. Fowler, eds. (Interscience, New York, 1960).
41. G. D. O'Kelley, *Detection and Measurement of Nuclear Radiation*, Oak Ridge National Laboratory, Rept. NAS-NS-3103 (1962).
42. W. Diethorn, *A Methane Proportional Counter System for Natural Radio-Carbon Measurements*, U. S. AEC Rept. NYO-6628 (1956).
43. P. Hopstone and S. Shalev, *Trans. Am. Nucl. Soc.* **21**, 132 (1975).

VRM/edas/lmc